HIGH-SPEED DUAL-WAVELENGTH OPTICAL POLARIMETRY FOR GLUCOSE SENSING

A Thesis

by

DANIEL TAYLOR GRUNDEN

Submitted to the Office of Graduate and Professional Studies of
Texas A&M University
in partial fulfillment of the requirements for the degree of

MASTER OF SCIENCE

Chair of Committee,	Gerard L. Coté
Committee Members,	Mary P. McDougall
	Prasad Enjeti
Head of Department,	Gerard L. Coté

May 2015

Major Subject: Biomedical Engineering

ABSTRACT

To non-invasively measure glucose concentrations across the aqueous humor of the eye, a high-speed, dual-wavelength optical polarimetric approach is proposed that addresses a key limitation of prior set-ups – system response time – while compensating for time-varying motion artifact due to corneal birefringence.

This research is made up of three goals. The first goal is to design and construct a high-frequency, ferrite core Faraday rotator that can both rotate and modulate linearly polarized light in a frequency range of 30 to 75 kHz. The second goal is to implement a single ferrite core Faraday rotator into the current polarimetric approach. The third goal is to replace three air-core Faraday rotators with two ferrite core Faraday rotators for both modulation and compensation, allowing for two different signals to be measured on a single photodetector.

In vitro phantom studies are performed with and without motion artifact. The sensor is shown to stabilize in ~2 msec and provide standard errors for glucose concentration of less than 13 mg/dL in the presence of motion. The results indicate that higher frequency modulation can reduce the overall system stabilization time with minimal loss of accuracy in the presence of motion artifact.

ACKNOWLEDGEMENTS

I would like to thank my committee chair, Dr. Gerard L. Coté, for his guidance, advice, and support through the course of this research. His professionalism and focus on various projects at the same time as performing his duties as department head have shown me the key qualities I strive for now and during my career. I couldn't have completed this work without him.

I would also like to thank my committee members, Dr. Mary P. McDougall and Dr. Prasad Enjeti, for their support and their time. Their guidance through theory and design pointed me in the right directions. Mr. Erwin Thomas III and Dr. Bilal Malik both guided me in new and interesting directions as well.

Thanks also go to my friends, including but not limited to Casey Pirnstill, Tony Akl, Zhen Fang, Brian Cummins, Haley Marks, Javier Garza, and Andrea Locke. They have all been helpful during these past few years.

Finally, I'd like to acknowledge my family, including but not limited to my mom, who never gave up on my education, my sister, who gave me the best advice and support, my brother, who has always supported me in whatever I do, and my girlfriend, who supported me when I needed it the most.

TABLE OF CONTENTS

Page

Page

LIST OF FIGURES

Page

Page

CHAPTER I

INTRODUCTION

Diabetes Mellitus

Diabetes mellitus is a metabolic disease in which production and/or effective use of insulin, the glucose-regulating hormone, is stunted. Diabetes mellitus is, therefore, characterized by high blood glucose levels. Glucose, also called dextrose, is a monosaccharide that is absorbed directly into the bloodstream during digestion. The anabolic hormone, insulin, regulates the transport of glucose from the bloodstream into the cardiac and skeletal muscle cells, fat cells, liver cells, and fibroblasts. Insulin is manufactured in the islets of Langerhans embedded in the pancreas.

Two classes of diabetes mellitus exist: primary and secondary. Primary diabetes originates from pancreatic inability or insulin resistance. Primary diabetes consists of three different types: Type I, Type II, and gestational diabetes mellitus (1). Type I diabetes, formerly called juvenile-onset or insulin-dependent diabetes, is an autoimmune response inside the pancreas. Specifically, this autoimmune response causes a reduction in the β-cells in the islet of the Langerhans, resulting in a stunted manufacture of insulin inside the pancreas and a total lack of insulin in the body. Type II diabetes occurs when too little insulin exists within the body or when the body's cells stop accepting the insulin pathway to move glucose into the cell. Gestational diabetes occurs in women with high glucose levels during pregnancy. The cause for gestational diabetes is unknown, but the current theory states that the placenta produces hormones for the

development of her baby; similar to Type II diabetes, these hormones can block the insulin pathway to move glucose into the cells.

In contrast, secondary diabetes originates from secondary causes, such as hormonal disease, insulin receptor abnormalities, genetic disorders, drugs, chemical agents, or toxins. Treatment of the antecedent diseases may prevent the need for glucose monitoring during secondary diabetes. Secondary diabetes may bring out primary diabetes in people who are predisposed.

Diabetes is a serious health issue. In 2012, 29.1 million people, or 9.3% of the U.S. population, had diabetes (2). Diabetes is ranked as the seventh leading cause of death in the United States (2). Diabetes complications include hypertension, heart disease, stroke, blindness and other eye problems, kidney disease, nervous system disease, dental disease, and amputation (1). Without proper therapy, glucose levels may fluctuate between 40 and 900 mg/dL. High blood glucose levels above 126 mg/dL when fasting or 200 mg/dL after meals (3) is called Hyperglycemia, which can damage the body's organs including the kidneys, eyes, nerves, and heart. In 2010, hyperglycemic crisis caused 2,361 deaths for adults over 20 years (2). In 2011, hyperglycemia caused about 175,000 emergency room visits for all ages (2). Low glucose levels below 72 mg/dL (4) is called Hypoglycemia, which may cause shock or death. In 2011, hypoglycemia caused about 282,000 emergency room visits for adults (1). Overall, the risk of death for people with diabetes is approximately double that of similarly aged individuals without diabetes (1). Thus, strict measurement and regulation of blood glucose concentrations is recommended up to five times per day (5).

Diabetes Therapy

The two common methods for glucose sensing are the Colorimetric and the Amperometric methods. These two methods are minimally invasive. In the original Colorimetric method, the color of the sample is simply compared with a color scale. Later in 1941, Miles Laboratories significantly improved the colorimetric method by including glucose oxidase (red-ox) and peroxidase. In 1964, Anton (Tom) Clemens developed a test strip (Dextrostix®), based on this colorimetric design, that could work with blood instead of urine. In 1979, Ames invented the first fingerprick lancet, Ames Autolet, for blood sampling. This minimally invasive method requires the patient to withdraw a small sample of blood from the interstitial tissue and apply the blood to a specially formulated test strip. As shown in **Equation 1**, Glucose oxidase and peroxidase are catalysts that break down the sugar into its metabolites. Glucose oxidase acts as a catalyst in the conversion of glucose to gluconic acid and hydrogen peroxide. Hydrogen peroxide is proportional to the glucose concentration.

$$Glucose + O_2 \xrightarrow{Glucose\ Oxidase} Gluconic\ Acid + H_2O_2 \quad (1)$$

When using the catalyst, Peroxidase, the peroxide oxidizes a chromophore or chromogenic substrate. Today, Tetramethylbenzydine causes a measureable color change as shown in **Equation 2**.

$$H_2O_2 + \underbrace{Tetramethylbenzydine}_{reduced,colorless} \xrightarrow{Peroxidase} \underbrace{Tetramethylbenzydine}_{oxidised,blue} + H_2O_2 \quad (2)$$

In 1985, Ames released the Glucometer® that could read the Dextrostix strip. This reflectance meter optically measures absorbance or the decrease in reflectance of the dye product in the test strip. It generates a numerical value that is representative of the color intensity in the reaction layer of the strip and thus the glucose concentration in the blood as well.

The Amperometric method for measuring glucose evolved in the mid-1950s. This method involves the reaction involving the oxidation of glucose. Leland Clarke proposed that a Platinum electrode can reliably measure oxygen changes if the electrode could be separated from the biological medium by a gas permeable membrane (6). The method was improved by immobilizing the glucose oxidase on a membrane, allowing glucose in the blood to directly react with the electrode. Currently, the electrode contains the enzymes, glucose oxidase or dehydrogenase, and the enzyme is deoxidized at the electrode generating an electric current (7, 8). The current is proportional to the glucose concentration in the blood. In 1974, Yellow Springs Instruments (YSI) released their Model 23 glucose analyzer using this method. In 1985, Cass described an amperometric based test strip (9). In 1987, Medisense launched the ExacTech® sensor incorporating this method. They deployed an exogenous mediator, such as ferrocene or Os(III), to accept electrons from the reduced enzyme. Amperometric detection has evolved overtime and now requires less blood, ~0.2 uL. Therefore, the sensing is less painful and measurements are faster.

Invasive glucometers are far from perfect, as they can be painful, cumbersome, embarrassing, and expensive. Repeated puncturing of the skin can lead to potential infection, and the disposal of test strips multiple times each day can potentially lead to dangerous chemical waste results. The sensors' reactions are time-dependent, with the reactions needing to complete before the blood is removed from the strip. Chemical interference and improper wiping can result in incorrect measure.

Noninvasive Glucose Sensing

Noninvasive glucose sensors measure the glucose concentrations without the need for the patient to draw blood, puncture skin, or potentially cause pain or trauma. In 2012, The National Center for Biotechnology Information published a review of ten noninvasive technologies for glucose sensing: bioimpedance spectroscopy (10-13), electromagnetic sensing (14-17), fluorescence technologies (18, 19), mid-infrared spectroscopy (20), near infrared spectroscopy (21-26), optical coherence tomography (27, 28), Raman spectroscopy (29, 30), reverse iontophoresis (31), ultrasound technology (32, 33), and optical polarimetry (34-47). They concluded that no technology has produced a single commercially viable sensor and that more research is required (48).

Optical polarimetry, which is the focus of this study, measures the rotation of linearly polarized light due to an increase in glucose. It is limited to measuring glucose in the eye due to the scattering properties of the skin. Eye movement and motion artifact provide a source of error. Other rotatory confounders present in the aqueous humor,

including proteins, ascorbic acid, and albuin, can provide a source for error. Optical polarimetry for glucose sensing is explained in more detail in the following section.

Glucose Sensing using Polarimetry

In the early 1800s, Jean Baptiste Biot discovered that a medium consisting of certain organic molecules, which he named optically active, cause transmitted linearly polarized light's plane of polarization to rotate (49). These optically active molecules lack a structural plane of symmetry and are called enantiomers or chiral molecules. Glucose is one such molecule. He described the interaction between the optically active medium and the transmitted polarized light using **Equation 3**:

$$[\alpha]_\lambda = \frac{\alpha}{LC} \tag{3}$$

where $[\alpha]_\lambda$ is the specific rotation of the optically active molecule at a given wavelength (λ) that is equal to the observed rotation (α) divided by the sample path length (L) and concentration (C) (49). Since the concentration of the optically active medium is in direct proportion to the linear rotation, sugar production industries started using optical polarimetry for monitoring glucose levels in the late 1800's (50).

In 1956, the sugar industry first became interested in Faraday modulation as a method to increase the root-mean-square function and stability of their optical

polarimeters for glucose sensing (51). This addition to the polarimeter has made the detection of small rotations due to physiological glucose levels possible.

In 1982, March and Rabinovitch first utilized optical polarimetry with the precision of the Faraday rotation for the purpose of non-invasive physiological glucose monitoring (34, 35). They chose the aqueous humor inside the eye, instead of skin, as a suitable sensing location due to its minimal scattering and depolarization.

In 1992, Cote et al. improved March and Rabinovitch's polarimeter by increasing its sensitivity for glucose-doped water solutions into the millidegree range. They implemented a true phase measurement technique that used a rotating linear polarizer for both linearizing and modulating the beam's polarization state (42, 52). That same year, Goetz et al. implemented an integrator into the feedback design and showed a micro-degree sensitivity (53, 54).

In 1994, King et al. utilized Pockels cells for modulation and compensation and implemented a multispectral polarimetric approach to minimize other optically active molecules in the aqueous humor (36). A year later, Michael implemented a polarimetric differencing technique into the multispectral polarimetric approach (55).

Also in 1994, Cameron et al. improved the accuracy and sensitivity with the implementation of a digital closed loop control system (43). In 1998, Coté et al. presented a dual-wavelength approach to minimize the effect of optical confounders and potentially motion-induced noise due to birefringence (56).

In the early 2000's, Ansari et al. and Rawer et al. proposed a polarimetric approach that used Brewster's reflection (57-59). In 2006, Cameron et al. utilized a

birefringence compensator to account for corneal birefringence during real-time polarimetric glucose sensing (60).

In 2010, Malik et al. proposed a closed-loop dual-wavelength polarimetric approach that could compensate for time-varying birefringence in eye phantoms (38). In 2012, Pirnstill et al. showed that dual-wavelength polarimetry can effectively reduce noise due to time-varying corneal birefringence *in vivo* allowing the accurate measurement of glucose concentration in the aqueous humor of the eye and correlating that with blood glucose (61). In 2013, Pirnstill et al. proposed a high-speed polarimetric method with decreased stabilization time; however, this single wavelength design was tested on a static glucose sample and did not account for time-varying birefringence (62).

The aforementioned research indicates that optical polarimetry has the potential to monitor glucose concentrations in the aqueous humor of the eye, but the approach's speed is limited. In this research, the optimization of the Faraday rotators and the signal separation method is proposed such that similar sensitivity from prior polarimeters can be provided with faster data-acquisition capability.

The research is made up of three goals. The first goal is to design and construct a high-frequency, ferrite core Faraday rotator that can both rotate and modulate linearly polarized light faster than the existing 1.09 kHz air-core Faraday rotator. The second goal is to implement a single ferrite core Faraday rotator into the current polarimetric approach. The third goal is to replace three air-core Faraday rotators with two ferrite core Faraday rotators for both modulation and compensation, allowing for two different

signals to be measured on a single photodetector. This new system significantly simplifies the system in terms of alignment and amount of signal at the detector by eliminating the need for an extra beam splitter, Faraday rotator, detector, and photodiode amplifier used in the optical setup.

CHAPTER II

THEORY

This section describes the theory to address the three research goals. In particular, this section overviews fundamentals of polarization and polarimetry, Jones calculus, optical activity, polarimetric glucose detection fundamentals, and system performance.

Polarization of Light Fundamentals

In this report, light is described as an electromagnetic wave. This transverse wave consists of both an electric and magnetic component orthogonal to each other. The wave's electric field vector, **E**, and magnetic field vector, **H**, are transverse to the direction of wave propagation. Usually, the electric component of the electromagnetic wave is used to describe the polarization vector of light. Polarized light occurs when the magnitude of the electric component of the light is aligned in a single direction. In other words, the light's vibrations occur in a single plane. Most sources of light are incoherent, randomly polarized, or partially polarized; the magnitude of the electric component of the electromagnetic wave randomly reorients itself in different directions. Polarizers are optical components that can reorient the direction of the electric component of the waves. Other states of polarization include elliptically and circularly polarized light. Elliptically polarized light occurs when the x-component of the linearly polarized light occurs out of phase of the y-component of the linearly polarized light when the light is

propagating in the z-direction. Circularly polarized light occurs when the x-component of the linearly polarized light occurs exactly 90 degrees out of phase of the y-component of the linearly polarized light. Humans, unlike some animals, cannot differentiate between different polarization states. Sensors, such as polarimeters, are therefore required to sense changes in polarization state.

Optical Polarimetry Fundamentals

Polarimetry, as shown in **Figure 1**, is the utilization of polarized light to measure light changes from different types of media. One example of light changes is from optical activity. Optical activity is due to the chiral molecules in the eye. These molecules rotate the plane of the linearly polarized light passing through the sample and will be discussed in greater detail later. To be a valid measurement device for polarimetry, it is necessary for light to be polarized. A polarizer is used to reflect the unwanted polarization states and pass only one plane of polarization. Although there are many types of polarizers, a reflective, linear polarizer is used to create polarized light to measure the aqueous humor glucose concentration in the anterior chamber of the eye. A second polarizer, called an analyzer, is rotated 90 degrees from the first polarizer. All light is reflected from crossed polarizers, unless there exists something between the two polarizers that changes the electric component state. The amount of change can be measured by the change in the intensity or color of the output beam. During glucose measurements, the first polarizer creates linearly polarized light. This light passes through the optically active sample, and a different polarization angle of transverse waves is created. The analyzer then passes

only rotated polarized light. The primary cause for the rotation is the concentration of aqueous humor glucose, chiral molecules correlated to blood glucose. The aqueous humor glucose concentration is then measurable.

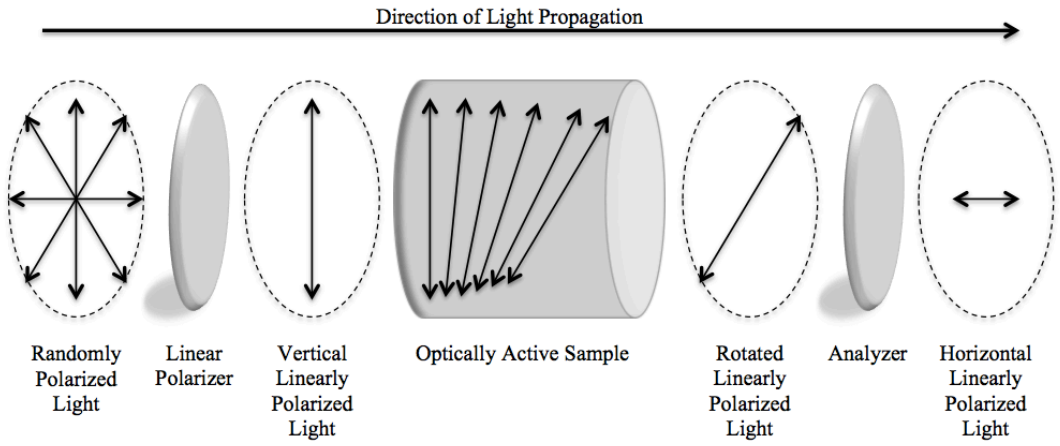

Figure 1. Basic polarimeter (63) comprised of two polarizers and an optically active sample placed between them.

Jones Calculus

The electric component of polarized light can be explained using Jones calculus. In 1941, R. Clark Jones devised a concise method to represent light, which he named the Jones vectors (64). These vectors only apply to polarized waves. Jones vectors, as shown in **Equation 4**, are written in column form and represent the electric field vector of light propagating along a path in the Z-direction.

$$\boldsymbol{E} = \begin{bmatrix} E_x(t) \\ E_y(t) \end{bmatrix} \quad (4)$$

where $E_x(t)$ and $E_y(t)$ are the instantaneous scalar components of the electric field, **E**, in the horizontal and vertical axis respectively. Jones Matrices represent linear optical elements in the path of the beam. These elements can affect the beam's polarization state and are represented by 2X2 matrices that mathematically perform operations on the Jones vector of an incident beam.

The block diagram of the optical components in a single wavelength polarimetric approach is shown below in **Figure 2**:

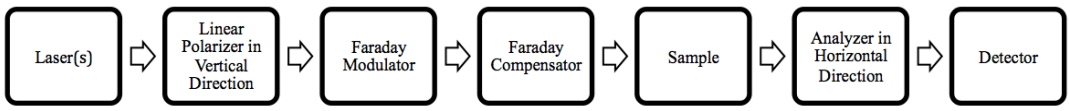

Figure 2. Block diagram for the single wavelength polarimetric approach for glucose sensing (43).

Goetz et al. showed that the output Jones vector describing the electric field at the detector is described by **Equation 5** (65). This vector is modeled as the product of Jones matrices of each individual element and the input Jones vector. The matrices are arranged opposite to the light propagation through each optical element. Goetz et al. reduced **Equation 5** to **Equation 6** (65).

$$\boldsymbol{E} = \begin{bmatrix} E_x(t) \\ E_y(t) \end{bmatrix} = \begin{bmatrix} 1 & 0 \\ 0 & 0 \end{bmatrix} * \begin{bmatrix} cos(\varphi_g) & -sin(\varphi_g) \\ -sin(\varphi_g) & cos(\varphi_g) \end{bmatrix} * \begin{bmatrix} \cos(\varphi_f) & -\sin(\varphi_f) \\ -\sin(\varphi_f) & \cos(\varphi_f) \end{bmatrix} \quad (5)$$

$$* \begin{bmatrix} cos\ (\theta_m sin\omega_m t) & -sin\ (\theta_m sin\omega_m t) \\ sin\ (\theta_m sin\omega_m t) & cos\ (\theta_m sin\omega_m t) \end{bmatrix} * \begin{bmatrix} 0 & 0 \\ 0 & 1 \end{bmatrix} * \begin{bmatrix} 0 \\ 1 \end{bmatrix}$$

$$I \propto \left(\phi^2 + \frac{\theta_m^2}{2} \right) + 2\phi\theta_m\, sin(\omega_m t) - \frac{\theta_m}{2} cos(2\omega_m t) \quad (6)$$

where I descries the intensity of the detected signal, ϕ represents the net rotation due to the optically active sample, θ_m represents the angular modulation depth from the Faraday rotation, and ω_m represents the Faraday modulation frequency in radians. A double-frequency ($2\omega_m$) component originates due to the half-shadow effect created by the perfectly crossed polarizers. **Equation 6** shows that without any optically active sample, the second term in the equation becomes zero and the detector shows only information at the double-frequency (2ω). When an optically active sample is introduced into the sensor, the detected signal becomes an asymmetric sinusoid, which contains both the fundamental frequency (ω) and double-frequency (ω) components. For the dual-wavelength approach, both beams pass through the same optical train. Thus, **Equation 6** can represent both wavelengths. Optical activity (discussed later) explains why two different intensities originate in **Equation 6** when two different wavelengths are used.

Optical Activity

Optical activity, also termed circular birefringence, rotates linearly polarized light. Louis Pasteur first realized that molecular symmetry is responsible for optical activity (66). Rotation of linearly polarized light occurs when the beam passes through a solution of chiral molecules. Glucose molecules are chiral and therefore rotate linearly polarized light. Left-handed and right-handed molecules rotate light differently. The equation describing the interaction of these chiral molecules with a light is represented by **Equation 3** where alpha is the observed rotation, C is the concentration of the optically active sample, L is the sample path length, and [α] is the specific rotation, which is dependent on the wavelength (λ), temperature and pH. This optical rotation is measurable through the use of polarimetry described above.

The wavelength dependence is described by using the modified Drude equation for wavelengths away from or between absorption bands of the media (67). Therefore $[\alpha]_\lambda$ can be described by **Equation 7**:

$$[\alpha]_\lambda = \frac{k_o}{\lambda^2 - \lambda_o^2} \tag{7}$$

where λ is the wavelength of interest, and k_o is a rotational constant corresponding to the wavelength, λ_o of maximal absorption. **Equations 3 and 7** explain that the observed rotation due to glucose is wavelength dependent.

System Performance

A lock-in amplifier extracts signals with a known carrier wave from a noisy environment. The output from the lock-in amplifier is configured to be proportional to the $2\phi\theta_m \sin(\omega_m t)$ component from **Equation 6** above. The lock-in amplifiers lock into the fundamental frequency and provide outputs correlated to the net rotation, ϕ, due to the optically active sample and Faraday compensators. A lock-in amplifier requires a strong reference signal at the same frequency as the frequency of interest. The input signal is multiplied by the reference signal, and the result is integrated over a specified period of time. This specific time period needs to be large enough (much larger than the signal period) in order to suppress unwanted noise. Therefore, the upper limit of the integration time from the lock-in amplifiers depends on the modulation frequency from the Faraday modulators. In other words, a higher Faraday modulation frequency provides the potential to create a faster output signal from the lock-in electronics, and a higher frequency modulation has the potential to improve the signal-to-noise ratio in the presence of motion artifacts (68).

It is possible to procure a more accurate and repeatable standard error by obtaining more data over a shorter period of time (62). The output from the lock-in amplifier is input into a proportional-integral-derivative (PID) controller for the controlled feedback into the Faraday compensators. This controller has three separate constant parameters. The proportional value, P, depends on the present error. The integral value, I, accumulates for past errors. The derivative value, D, predicts future errors. For this optical polarimeter, the PID controller takes at least five lock-in amplifier

time-constants to stabilize the feedback control system. The faster the lock-in amplifier's time constant, the faster the overall system can stabilize. The overall stabilization time also depends on the sampling rate. Experiments have shown that overall stabilization time is at least ten times the sampling time. The faster the sampling rate, the faster the overall system stabilization time.

Since every optical component in an optical train deteriorates the optical signal slightly, the reduction of parts improves the signal at the detector. A 50:50 beam splitter creates, on average, a 50% loss in signal at one of the detectors, with 50% of the light intensity transmitted and 50% of the light reflected. The optical signal in the dual-wavelength polarimeter is split into two different detectors. As shown in **Equation 6**, the polarimetric approach for glucose sensing signal depends on the intensity of light on the detector. Because half the intensity reaches the detector, more amplification is required, potentially creating a source for noise.

CHAPTER III

MATERIALS AND METHODS*

This section describes the materials and methods to address the three research goals.

Goal 1: Faraday Rotator Development

As described by Malik et al. and Pirnstill et al., one method for creating a dual-wavelength polarimeter includes Faraday modulation and lock-in electronics that produced sub-millidegree sensitivity (38, 61). The lock-in amplifiers' speed, or system response time, has a minimum that depends on the Faraday modulation frequency to suppress unwanted noise including the double-frequency term. Put another way, a faster Faraday modulation frequency allows for a faster overall system response time.

Air Core Faraday Modulator Analysis

The air-core Faraday rotation techniques used in previous studies for glucose sensing are limited to direct current (DC) and low frequency alternating current (AC) applications (39, 61, 69). This air-core Faraday modulator, as shown in **Figure 3**, consisted of a bobbin of more than 3000 turns of 23 AWG wire wrapped around a Terbium Gallium Garnet (TGG) crystal. The impedance of the coil was high in the frequency region of interest (30 to 75 kHz). The impedance and self-resonant frequency of the air-core Faraday modulator were therefore measured in an attempt to find why the impedance

* Part of this chapter are reprinted with permission from D.T. Grunden, C.W. Pirnstill, and G.L. Cote, "High-speed dual-wavelength optical polarimetry for glucose sensing," *SPIE Photonics West* 895111-895111-895116 (2014). Copyright 2014 SPIE.

was high. A voltage drop across a 10kΩ resistor placed in series with the coil provided the information needed.

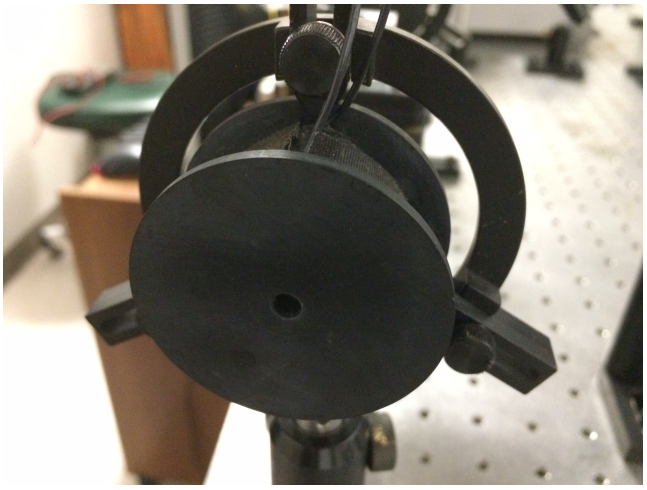

Figure 3. Air core Faraday modulator.

Ferrite Core Faraday Modulator Development and Analysis

Three ferrite core Faraday rotators were developed for high-frequency modulation of linearly polarized light in the frequency range of 30 to 75 kHz. The ferrite C-shaped core, as seen below in **Figure 4**, made up the bulk of the Faraday rotator.

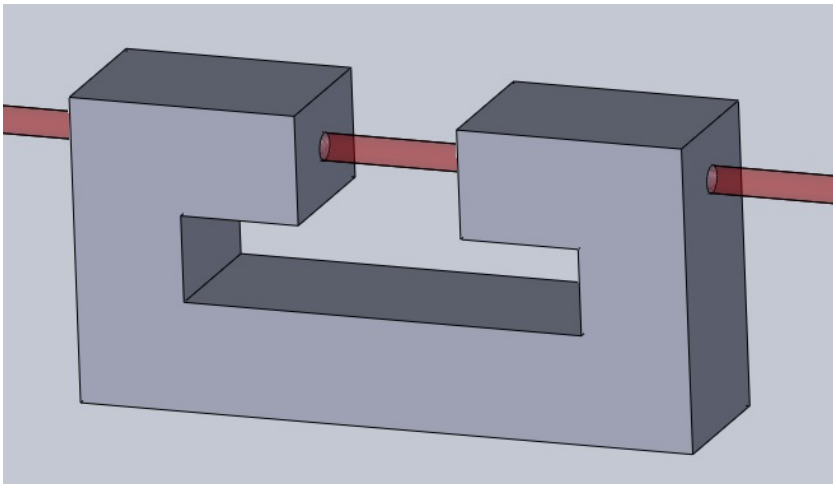

Figure 4. Ferrite core CAD rendering illustrating optical beam passing through core.

The cores were custom machined by ELNA Magnetics and are described in detail by Pirnstill et al. (70). The device properties depend on the geometry of the magnetic core, the size of the air gap, the properties of the core material, and the operating temperature of the core. As a result, the Faraday rotator's core properties could be optimized for either large magnetic field generation or a large range of modulation frequencies (71, 72). The overall lengths of these cores were ~57 mm, the heights were ~28 mm, and the widths were ~14 mm. The ferrite core was made from a magnetic material with a high permeability that confined and guided the magnetic flux densities. A 3D printed ferrite core holder was used to prevent magnetic flux density coupling between the ferrite core and the metal optics components. The ferromagnetic core was comprised of a low-loss MnZn ferrite designed for high flux power applications at frequencies up to 200 kHz due to the atomic properties of the ferrite (70). A through-hole (~2.5mm in diameter) lied within the core as seen in **Figure 4** for light to travel

through. A magneto-optic cylinder (~11 mm in length) lied inside the gap (~15 mm in length) of the C-shaped ferrite core Faraday rotator. Both the optical clarity and the large Verdet constant of approximately 134 rad/T/m for 632 nm made Terbium Gallium Garnet (TGG) crystal (Deltronic Crystals Inc., Dover, NJ) a good choice for this magneto-optic rod. TGG crystal has approximately twice the Verdet constant of terbium-doped glass. A coil was wrapped around the side of the gapless side of the C-core, and current was supplied into the coil. A resulting magneto-motive force (MF) propagated around the C-core and through the gap containing the TGG crystal. Similar to the air cores, the MF inside the TGG crystal rotated the plane of polarization (β) of the light beam travelling through the crystal. **Equation 8,** below, shows that the rotation results from the product of the crystal's Verdet constant (V), the magnetic flux density (B) inside the crystal, and the crystal's length (L). The AC signal through the coiled wire generated an alternating magnetic flux density (±B) inside the crystal.

$$\beta = VBL \tag{8}$$

Different types of Litz wire and a different number of turns around the ferrite core were used to provide larger magnetic flux densities across the TGG crystal due to the decrease in the skin effect and proximity effect at the proposed frequencies (73). At high frequencies in and above the kHz range, current is carried mainly on the surface of wire. This smaller volume for current to flow causes the wire's resistance to increase above its DC value. Litz wire mitigates this issue, since it is made of smaller, thinner,

insulated, parallel strands of wires intertwined so no wire is near the surface or the interior. As a result, the skin effect and AC resistance of the overall wire were reduced, and larger currents could flow at frequencies in the kHz range. Proximity effect occurs when current flows in loops due to the magnetic fields generated by nearby wire. Litz wire reduces proximity effect by the twisting or weaving of the strands. The twisting and weaving ensures that each strand has equal current. A 3D printed litz wire holder was used to prevent shorts along the wire against the sharp edges of the ferrite core.

Two experiments were performed to find a number of windings around the ferrite core that provided sufficient magnetic flux density and optical rotation of linear polarized light in the frequency range of 30 to 75 kHz. The first experiment measured the self-resonant frequency of three different ferrite cores wrapped with three different number of turns of 30 strands of 38-gauge wire: 91, 101, and 324 turns. **Figure 5** describes that the inductor (comprised of the three different coils) was the variable of interest. The second experiment measured the impedance of a single winding (101 turns) around a single ferrite core with three different capacitors placed in series with this coil. **Figure 6** describes that three different series capacitors made up the variable of interest. A voltage drop across a resistor placed in series was used to measure the impedance and SRF of each coil for each experiment.

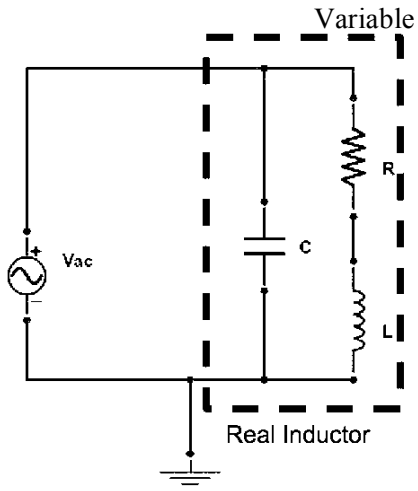

Figure 5. Real inductor with three different number of turns. The inductor itself is the variable of interest. A range of frequencies was sent through the coil to provide a frequency response of each coil's impedance.

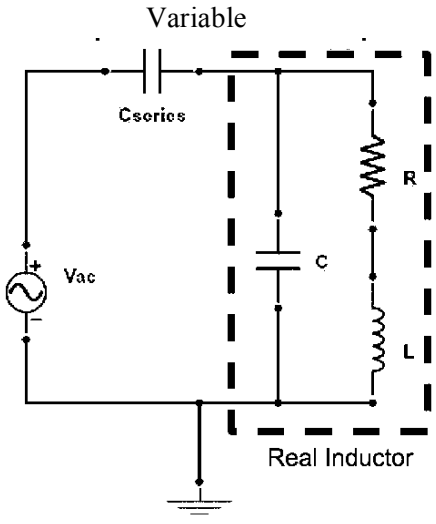

Figure 6. Three capacitors were placed in series with a single 101-turn coil to tune the coil to resonate at three different frequencies.

After ~100 turns provided a SRF outside of the frequency range of interest, the number of individual strands of the litz wire was increased. The method for measuring alternating magnetic flux density of the ferrite core Faraday rotator and, therefore, the alternating rotation of the linearly polarized light is described below. **Equation 8** provides the optical rotation based on the magnetic flux density achieved. As previously stated, the Verdet constant of TGG crystal is calculated to be approximately 134 rad/T/m for 632 nm light. The magnetic flux density created by the current flowing through the coil wrapped around the C-core was measurable by using a custom built Trifield AC Gaussmeter (AlphaLab Inc., Salt Lake City, Utah). The length of the TGG crystal was measured with calipers and approximated 11.0 mm. Therefore, a magnetic flux density of ±17 mT inside the C-core gap provided ±1 degree of rotation. The inductors were tuned with capacitors placed in series with the inductor to maximize the current flowing through the device at frequencies ranging from 30 to 75 kHz. A Wideband Power Analyzer Model 2335A (Clarke-hess, Medford, NY) was used to measure the voltage, current, and total power flowing through the coil.

DC Compensation

The novel Faraday rotators were constructed with both modulation and compensation in mind. Different approaches were attempted to create both an AC and DC magnetic flux density through the crystal without coupling either signal into the other source. The first method, shown in **Figure 7**, included a modified bias-tee circuit to provide both an AC and DC signal through the same coil. The bias-tee circuit used a

Hammond 193S inductor ($L_{BiasTee}$) with an inductance of 1.0 H to block the AC signal from flowing into the DC source (V_{dc}). The series resonant capacitor (C_{series}) tuned the Faraday rotator and blocked the DC signal from flowing into the AC source (V_{ac}). The second method, shown in **Figure 8**, used two different coils wrapped in various sections around the ferrite core and/or crystal to create both an AC and DC magnetic flux density across the TGG crystal. L_{AC} and L_{DC} represent the coils for modulation and DC compensation respectively. R_{DC} represents the resistor placed in series with the DC compensation coil.

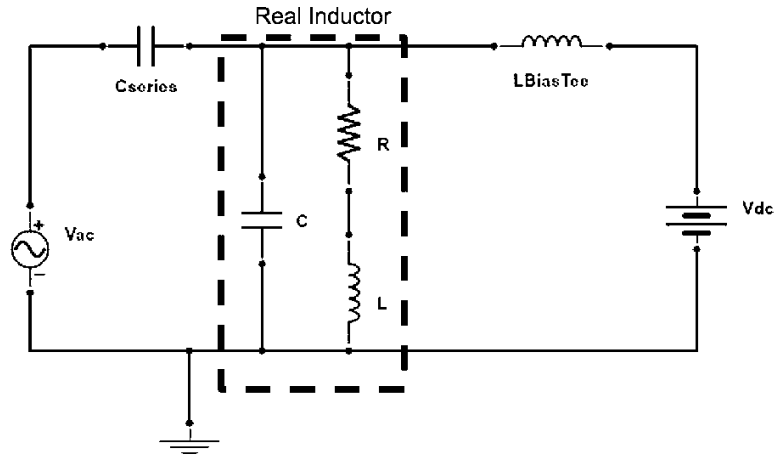

Figure 7. Modified bias-tee to send both an AC and DC signal through the coil simultaneously.

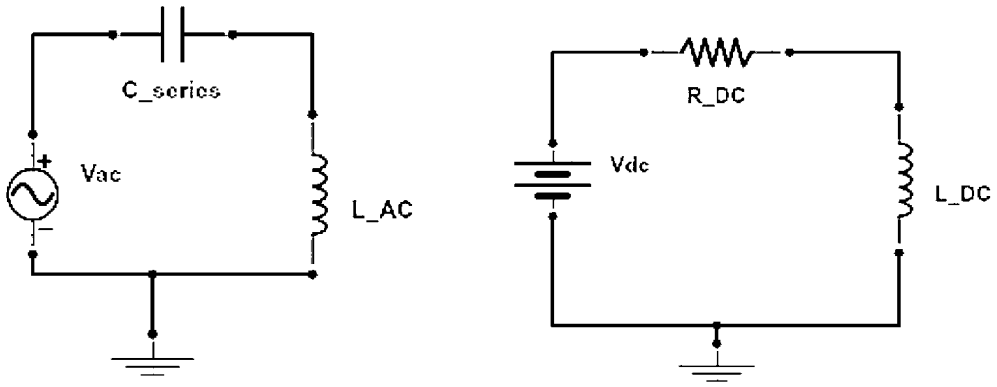

Figure 8. Two circuits and coils provide both modulation and compensation on a single core.

The AC magnetic flux density was measured using the Trifield AC Gaussmeter. The DC magnetic flux density was measured using a basic polarimeter, which consisted of a laser source, two crossed polarizers, a detector, and the Faraday rotator.

Goal 2: Dual-Wavelength Polarimeter with a Single Ferrite Core Faraday Modulator

The dual-wavelength approach has been proven to reduce and potentially eliminate the effect of time-variant corneal birefringence (38). The dual-wavelength optical polarimetric approach used here consisted of a single high-speed Faraday modulator and dual polarimetric optical compensators for a closed-loop configuration. The high-frequency, dual-wavelength approach is shown in detail in **Figure 9** and is described in detail by Grunden et al. (74).

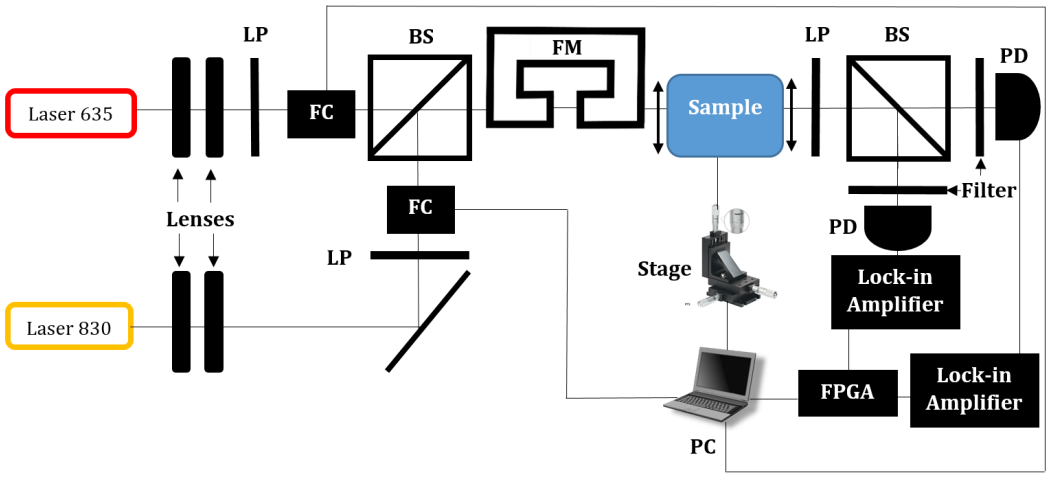

Figure 9. Schematic illustrating experimental setup of the high-speed closed-loop dual-wavelength optical polarimeter utilizing a single Faraday-modulation frequency.

Two laser diodes (Power Technology, Inc., Little Rock, Arkansas) emitted wavelengths of 635 nm and 830 nm with emission power of 7 mW and 20 mW respectively. These two beams were minimized and collimated with a converging and diverging lens for passing the beams through the Faraday modulator (FM) with minimal losses, scattering, and diffraction. 1:100,000 Glan-Thompson linear polarizers (LP) (Newport, Irvine, California) then linearly polarized the two beams in the horizontal orientation. The two linearly polarized beams passed through two in-house built air-core Faraday rotators (FC) that provided compensation for closed-loop operation. This polarimetric approach consisted of two air-core Faraday rotators for compensation and one ferrite core Faraday rotator for modulation. These air-core Faraday rotators were constructed from TGG crystals (Deltronic Crystals, Inc., Dover, New Jersey) inside bobbins wound with electric coils.

After a beamsplitter/combiner (BS) (Optosigma Corp., Santa Ana, Califormia) combined the two linearly polarized beams, the polarization vector of both beams was modulated using the ferrite core Faraday modulator (FM). This approach replaced the previously used slower air-core Faraday modulator operating at 1.09 kHz (38, 62) with the faster ferrite core Faraday modulator operating at a frequency between 30 and 75 kHz. For this aim, a combination of 3 capacitors yielding a net capacitance of 7.85 nF were placed in series with the ferrite core Faraday modulator for Series Resonance at 37 kHz modulation frequency. The Faraday modulator was powered by an OPA548F operational amplifier and switching power supplies (Dell, Round Rock, TX) to produce a modulation depth of ~±1 degree. The OPA548F has a fast frequency response (1 MHZ Gain-Bandwidth Product) and current throughput (3A Continuous). The Faraday modulator consumed ~2.4 W of power. As described above, the Faraday modulator was built from a high permeability ferromagnetic core to enhance the amplitude and uniformity of the magnetic flux density produced across the air gap, which contained a TGG crystal (70).

After the beams propagated through the ferrite core Faraday modulator, the two beams passed through a quartz cuvette (Sigma, St. Louis, MO) containing varying glucose concentrations in the physiological range of 0-600 mg/dL for sensitivity experiments. Later, the cuvette was placed on a computer-programmable translation stage (Thorlabs, Newton, NJ) for motion artifact studies at frequencies similar to those that resemble human cardiac and respiratory cycles. The sample was shifted up 0.5 mm and then down 0.5 mm with a velocity of 1 mm/sec.

Following the sample, a second linear polarizer (analyzer), oriented perpendicular to the initial polarizers, transmited only rotation and birefringence information. A second beamsplitter/combiner and bandpass filters then split the two beams before the photodetectors. Two photodiodes (PD) (Thorlabs, Newton, NJ) followed by two wide-bandwidth amplifiers (Melles-Griot, Albuqurque, New Mexico) transduced and amplified the two beams separately. The two signals were then fed into two lock-in amplifiers (Standord Research Systems, Sunny-vale, California) utilizing a 1 msec time-constant. Lock-in amplifiers are described in more detail in CHAPTER II.

A field-programmable gate array (FPGA) based feedback proportional-integral-derivative (PID) controller, programmed in Labview 10.0 32-bit (National Instruments, Austin, Texas) provided near real-time closed-loop feedback to the Faraday Compensators. Multiple-linear regression (MLR) analysis, which is analogous to scaled subtraction, can accommodate for the birefringence. Therefore, **Equation 12** can potentially predict glucose in the presence of motion artifact. The detected signal, *I*, on the photodetector provided signal at the fundamental frequency, ~37 kHz, only when optical activity or birefringence was introduced between the two linear polarizers. Similar to Malik et al, the dual-wavelength and MLR approach were used to extract the rotation due to optical activity (75). Two wavelengths were used to compensate for the time-varying birefringence.

Goal 3: Dual-Wavelength Polarimeter with Dual Ferrite Core Faraday Modulators

Similar to the dual-wavelength polarimeter with a single ferrite core Faraday modulator, **Figure 10** describes the new optical polarimeter using two ferrite core Faraday rotators to modulate the two different beams at two different frequencies.

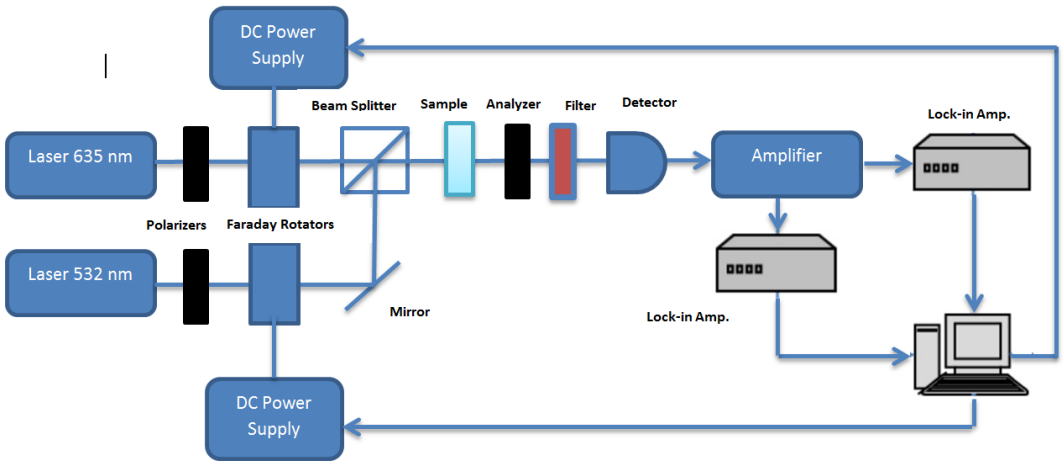

Figure 10. Schematic illustrating experimental setup of the high-speed closed-loop dual-wavelength optical polarimeter utilized dual-Faraday modulation frequencies.

Two laser diodes (Power Technology, Inc., Little Rock, Arkansas) emitted two different wavelengths at 635 nm and 532 nm with emission powers of 7 mW and 10 mW respectively. The 830 nm wavelength laser from the second goal was switched to the 532 nm wavelength for this goal, because the 532 nm wavelength laser creates a larger rotation due to optical activity and Faraday effect than the 830 nm wavelength laser. The 1:100,000 Glan-Thompson linear polarizers (Newport, Irvine, California) linearly polarized the two beams in the horizontal orientation. Unlike the single modulation approach, this polarimetric approach consisted of two ferrite core Faraday rotators that

could compensate and modulate on a single device for each wavelength. The 635 nm laser beam was modulated at ~73.6 kHz, and the 532 nm laser beam was modulated at ~52.2 kHz, both with a modulation depth of ~±1 degree. 100 turns of 125/40 litz wire was wrapped around the C-core of the Faraday rotator for modulation. 20 turns of 24 Gauge wire was wrapped around the TGG crystal residing inside the gap of the C-core for DC compensation. Four OPA548F operational amplifiers configured in non-inverting linear gain setups supplied power to the four different coils, two for modulation and two for DC compensation.

A beamsplitter/combiner (Optosigma Corp., Santa Ana, California) then combined the two modulating linearly polarized beams. The two beams passed through a quartz cuvette (Sigma, St. Louis, MO) containing varying glucose concentrations in the physiological range of 0-600 mg/dL.

Following the sample, a second linear polarizer (analyzer) oriented perpendicular to the initial polarizers supplied only rotation and birefringence information. Unlike the single frequency approach, a second beamsplitter/combiner and bandpass filters were not needed to optically separate the two beams before the photodetectors. Therefore, a single photodiode (PD) (Thorlabs, Newton, NJ) followed by a single wide-bandwidth amplifier (Melles-Griot, Albuqurque, New Mexico) transduced and amplified the two beams together. The two signals were then fed into two lock-in amplifiers (Stanford Research Systems, Sunny-vale, California), both utilizing a 100 usec time-constant. This time-constant was ten times faster than the 1 msec time-constant used in the single modulator approach. The SR850 Lock-in amplifier was tuned to the 73.6 kHz signal and filtered

noise and the signal at 52.2 kHz. The SR830 Lock-in amplifier was tuned to the 52.2 kHz signal and filtered noise and the 73.6 kHz signal.

The same field-programmable gate array (FPGA) based feedback proportional-integral-derivative (PID) controller, programmed in Labview 10.0 32-bit (National Instruments, Austin, Texas) provided closed-loop feedback to the Faraday Compensators

As a result of these two frequencies, a single detector replaced the beam splitter and two detectors shown in **Figure 10**. A Melles Griot Photodiode Amplifier was also removed. The single detector passed both the 635 nm and 532 nm laser beams and converted these two optical signals into electrical signals. Then the single photodiode amplifier amplified both signals. The output of the photodiode amplifier was split into the two Lock-in amplifiers. The two air-core Faraday rotators for DC compensation were no longer required, because the Faraday compensation now occurs in the same crystal responsible for Faraday modulation.

The sensor's sensitivity was determined by three runs of static glucose concentrations varying from 0-600 mg/dL in increments of 100 mg/dL for both wavelengths similar to testing described by Malik et al. (38). These sensitivity experiments were performed without motion. Later, the cuvette was placed on a computer-programmable translation stage (Thorlabs, Newton, NJ) for motion artifact studies. Noise was simulated at a frequency of 0.33 Hz and simulated respiration at 20 beats per minute.

CHAPTER IV

RESULTS AND DISCUSSION*

This section outlines the results with discussion for each research goal.

Goal 1: Faraday Rotator Development

For the first research goal, a high-frequency, ferrite core Faraday rotator, that modulated and rotated linearly polarized light in a frequency range of 30 to 75 kHz, was developed.

Air Core Faraday Modulator Analysis

This section describes the high impedance of the air core Faraday modulator. The impedance, Z_L, of an inductor modulated at a frequency is shown in **Equation 9**.

$$Z_L = \sqrt{R_{AC}^2 + X_L^2} \tag{9}$$

The impedance depends on the inductor's AC resistance, R_{AC}, and reactance, X_L. This reactance, as shown in **Equation 10**, increases with frequency (f) and inductance (L).

$$X_L = 2\pi f L \tag{10}$$

* Part of this chapter are reprinted with permission from D.T. Grunden, C.W. Pirnstill, and G.L. Cote, "High-speed dual-wavelength optical polarimetry for glucose sensing," *SPIE Photonics West* 895111-895111-895116 (2014). Copyright 2014 SPIE.

The inductance for any coil of wire can be approximated by **Equation 11**.

$$L = \frac{N^2 \mu A}{l} \tag{11}$$

where L is the inductance of the coil, N is the number of turns of the coil, μ is the permeability of the core, A is the area of the coil, and l is the average length of the coil.

Although an increase in the inductor's number of turns increases its inductance and therefore its reactance and magnetic flux density generation, all real inductors have parasitic capacitance between the windings of the coil. A coil's self-resonant frequency (SRF) exists when parasitic capacitance of the coil resonates with the coil's inductance at a specific frequency. At this specific frequency, the SRF, the capacitance resonates with the inductor's inductance, L, creating, in essence, a parallel resonant tuned circuit. A coil's SRF can be calculated using **Equation 12** below:

$$SRF = \frac{1}{2\pi\sqrt{LC_{par}}} \tag{12}$$

As previously mentioned, the coil's inductance (L) is a function of the number of turns, but the parasitic capacitance (C_{par}) is a function of how well the coil is wound. Parasitic capacitance exists when two conductors at different potentials are in close proximity to one another and affect each other's electric field.

As shown in **Figure 11**, the air core Faraday modulator had a SRF of 40 kHz; as a result, there existed large impedance in the frequency range of interest.

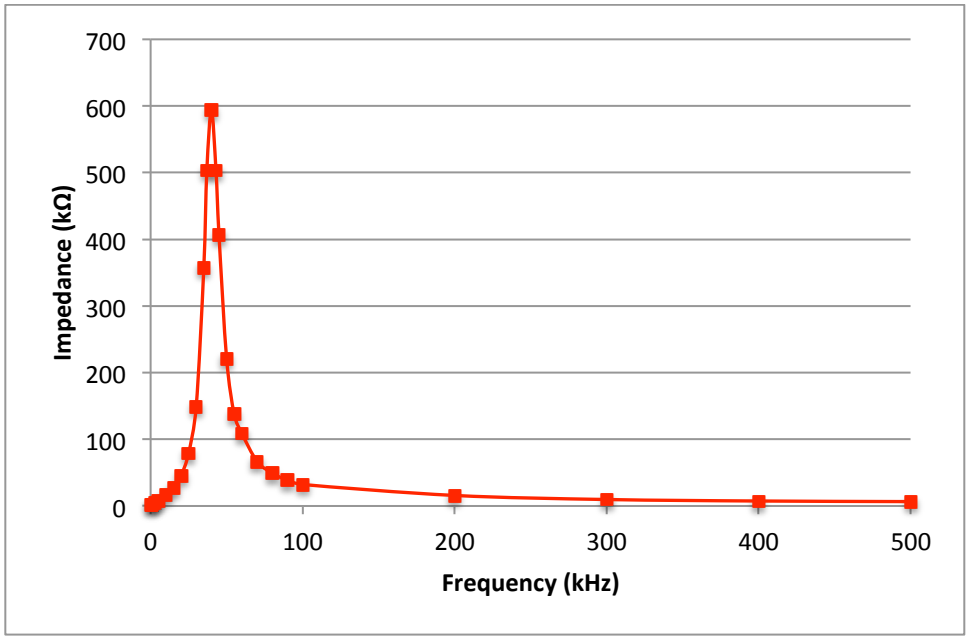

Figure 11. Self-resonance for the air core Faraday rotator.

Ferrite Core Faraday Modulator Development and Analysis

Because the air core Faraday modulator provided a high impedance and SRF in the frequency range of interest (30 to 75 kHz), a new ferrite core Faraday rotator was developed for high frequencies. The core was first wrapped with three different numbers of litz wire. This first experiment consisted of measuring the SRF of three different number of windings of 30 strands of 38-gauge wire. **Figure 12** shows that a decrease in the number of turns around the core caused the Faraday rotator's SRF to increase and the overall impedance inside the desired frequency range of 30 to 75 kHz to decrease.

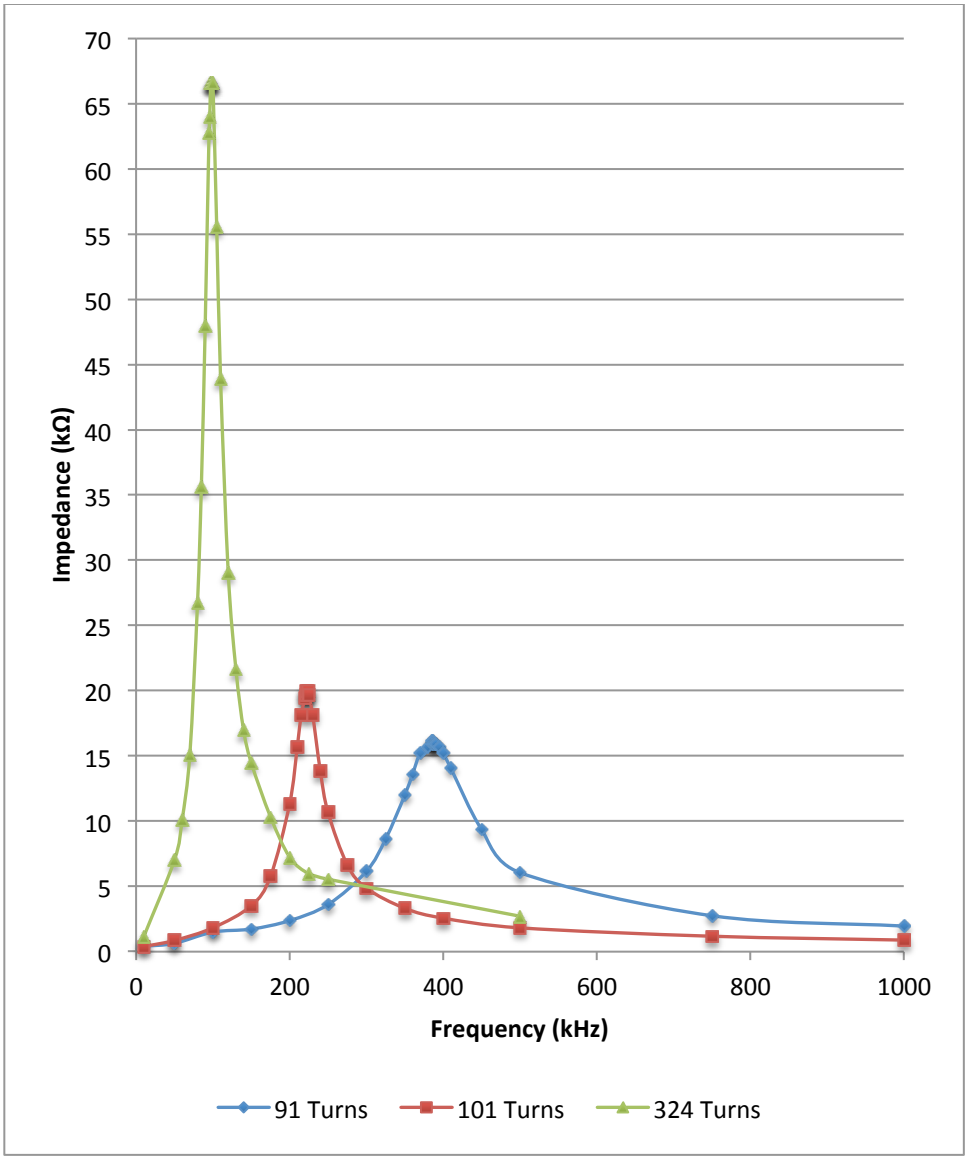

Figure 12. Self-resonance for various windings (91 turns, 101 turns, and 324 turns) of 30 strands of 38-gauge litz wire.

The 324, 101 and 91-turn coils each had a SRF of ~98.5, ~223, and ~389 kHz respectively. At frequencies above the inductor's self-resonant frequency, parasitic capacitive effect appeared to dominate, and the overall impedance of the inductor decreased.

During the series resonance experiment, three different capacitors are placed in series with the 101-turn coil. During series resonance, the inductor's reactance dropped to zero at a specific, tuned frequency. The inductor's resulting minimized impedance (Z_L) at the tuned frequency is shown in **Equation 13**.

$$Z_L = R_{AC} \tag{13}$$

The inductor's resulting impedance at the tuned frequency is theoretically equal to the inductor's AC resistance (R_{AC}) at the tuned frequency. **Figure 13** shows the 101-turn coil's impedance with various capacitors placed in series for series resonance. The 101-turn coil was chosen over the other two coils, because during the previous SRF experiment that compared the three coils with different windings, the 101-turn coil provided similar impedance in the frequency range of interest while having a higher SRF than the 91 turn coil.

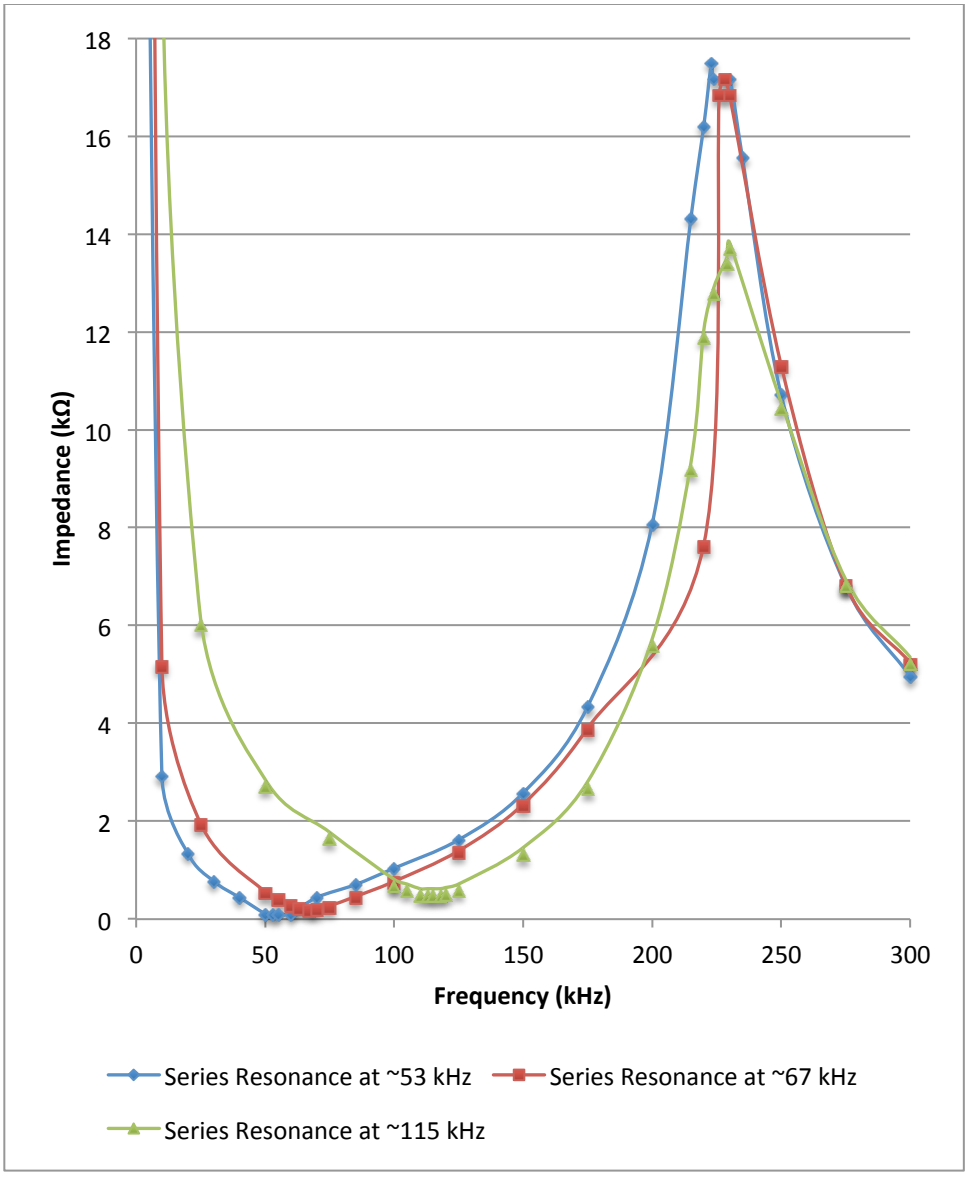

Figure 13. Series-resonance frequency response of the 101-turn litz wire tuned to various frequencies.

As shown, the impedance at series resonance increased with an increase in the series resonance frequencies, especially when the tuned frequency approached the coil's SRF. The 101 turn coil could achieve series resonance of ~473 ohms at ~115 kHz while the

324 turn coil could only achieve ~447 ohms at ~16 kHz. A series resonance near the coil's SRF increased power consumption.

The number of individual strands was then increased. The increased number of strands allowed for a larger current to flow while keeping the coil's SRF out of the 30 to 75 kHz frequencies of interest. The magnetic flux density is a function of both the number of turns and the current flowing through the coil. As shown in **Figure 11**, a decrease in the number of turns increased the coil's SRF, but MFD is a function of the number of turns and current. With fewer turns, more current was required to flow for a given MFD. 100 turns of 125 individually stranded 40-gauge AWG wires (type SPNSN 125/40 served litz wire, MWS Industries) was chosen due to the previous 101 turn coil providing the highest SRF and lowest AC resistance in the desired frequency range of 30 to 75 kHz. More strands allowed more total current to flow. For one specific frequency inside the 30 to 75 kHz frequency range, ~2.4 W created ±17 mT and thus ±1 degree of rotation at ~37 kHz during series resonance. The air-core Faraday modulator required ~1.92 W to generate ±1 degree of rotation at ~1 kHz during series resonance. The ferrite core Faraday rotator had an inductance of ~2 mH compared to the ~200 mH air core inductors.

Implementation of DC Compensation Inside the Faraday Rotator

Two methods were created to simultaneously modulate and compensate the linearly polarized light using a single ferrite core based Faraday rotator. The first method to send both an AC and DC signal through the coil included a purely electric design.

After experimenting with the purely electric bias-tee circuit shown in **Figure 7**, the inductor did not provide enough impedance to completely block the AC signal from flowing into the DC source. A decrease in AC MFD resulted across the crystal.

A new method was, therefore, developed to create both an AC and DC MFD across the TGG crystal. A 20-turn coil was wrapped around the crystal, which resided inside the core's gap. The coil did not touch the ferrite core to reduce coupling of AC and DC signals. 23-gauge wire was chosen, because this gauge allows a maximum of 4.7 amps of DC signal. Also, standard AWG wire can potentially help prevent AC from flowing through the DC compensation circuit. A 10-ohm resistance was used in series with the 20-turn coil to increase the DC circuit impedance. With the resistor in place, this coil required ~14 W to produce 1 degree of DC rotation, but the resistor effectively blocked the coupling of the AC signal from the 100-turn coil in the frequency range of 30 to 75 kHz.

Ferrite Core Faraday Rotator Concluding Statement

In summary, a high-frequency, ferrite core Faraday rotator – that modulated and rotated linearly polarized light in a frequency range of 30 to 75 kHz – was effectively developed. Wrapping a ferrite C-shaped core with 100 turns of litz wire for AC modulation and 20 turns of AWG wire for DC compensation appeared to produce reasonable results for this Faraday rotator. Preliminary studies showed that the lock-in amplifiers in the polarimetric glucose sensor could lock into the signal inside the frequency range of 30 to 75 kHz (62); also, there was ~4 degrees Celsius increase in

temperature in the coil over 50 minutes. A box, as shown in **Figure 14**, was placed around the Faraday rotator to help isolate the device from temperature fluctuations in the environment.

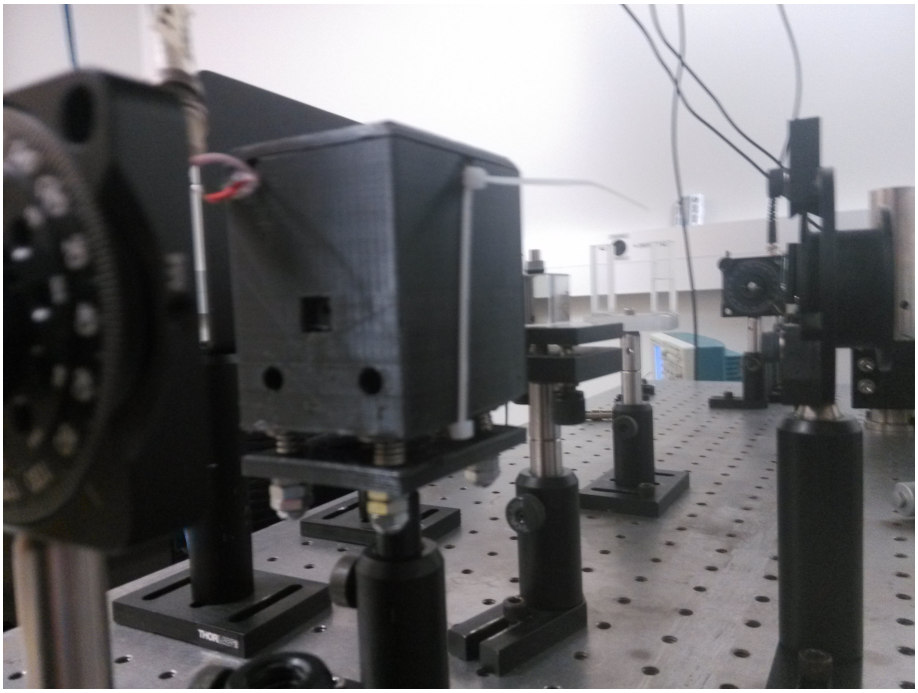

Figure 14. Ferrite core Faraday modulator box in optical setup.

Goal 2: Dual-Wavelength Polarimeter with a Single Ferrite Core Faraday Modulator

For the second research goal, the 1.09 KHz air-core Faraday rotator in the dual-wavelength optical polarimetry setup described by Malik et al. (39) was replaced with a new ferrite core Faraday rotator for modulation only. The ferrite core Faraday rotator, shown in **Figure 9**, could drive faster modulation frequencies than the air-core Faraday rotator used in previous designs (38, 61). Faster modulation frequencies and the resulting faster Lock-in amplifier's time constant settings decreased the overall speed of the closed-loop system response and sensor reading. The air-core Faraday rotators used in the previous dual-wavelength approach described by Malik et al. could only modulate light at 1.09 kHz; therefore, the lock-in amplifiers required a slow 100 msec time constant setting, and the system resulted in a 300 msec stabilization time for the overall response time for his sensor (38). More recently, Malik et al. and Pirnstill et al. performed *ex vivo* and *in vivo* studies with a 100 msec stabilization time (39, 61). The dual-wavelength polarimetric closed-loop approach in **Figure 9** was designed and is described in detail by Grunden et al. (74). It consisted of a Faraday modulation frequency of ~37 kHz, a lock-in amplifier time-constant setting of 1 msec, and a system response stabilization time of less than 10 msec.

Sensitivity Experiments

To test the repeatability and accuracy of the device, data processing without motion was performed and is described in detail by Grunden et al. (74). A linear

regression model of the data acquired from the high-speed dual-wavelength polarimeter with a single Faraday modulation frequency provided a standard error of 20.3 and 10.0 mg/dL for the 635 and 830 nm wavelengths respectively. The high error in the 635 nm wavelength laser may have been due to a misalignment of the system. The 635 and 830 nm wavelengths provided correlation coefficients of 0.992 and 0.998 respectively. **Figure 15** shows MLR of the data without motion. The MLR reduced the standard error to 9.43 mg/dL and improved the correlation coefficient to 0.999.

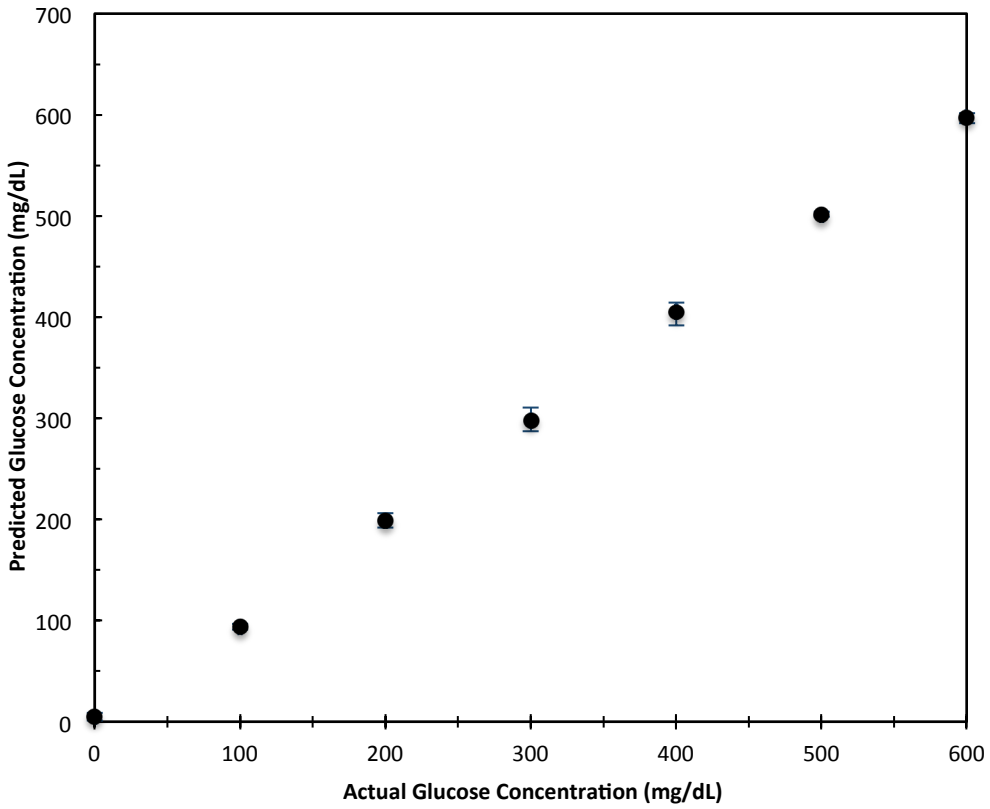

Figure 15. Predicted glucose concentration as a function of actual glucose concentration for 635 nm and 830 nm dual-wavelength approach from 0-600 mg/dL without motion.

Experiments with Motion Artifact

Dual-wavelength sensitivity studies with motion, reported by Malik et al. resulted in 14.5 mg/dL error with a correlation coefficient of 0.998 (76). Static glucose concentrations between 0-600 mg/dL with 100 mg/dL increments determine the sensor's repeatability and accuracy in the presence of motion artifact. **Figures 16** and **17** show the predicted glucose concentrations as a function of the actual glucose concentrations for wavelengths 635 nm and 830 nm (74).

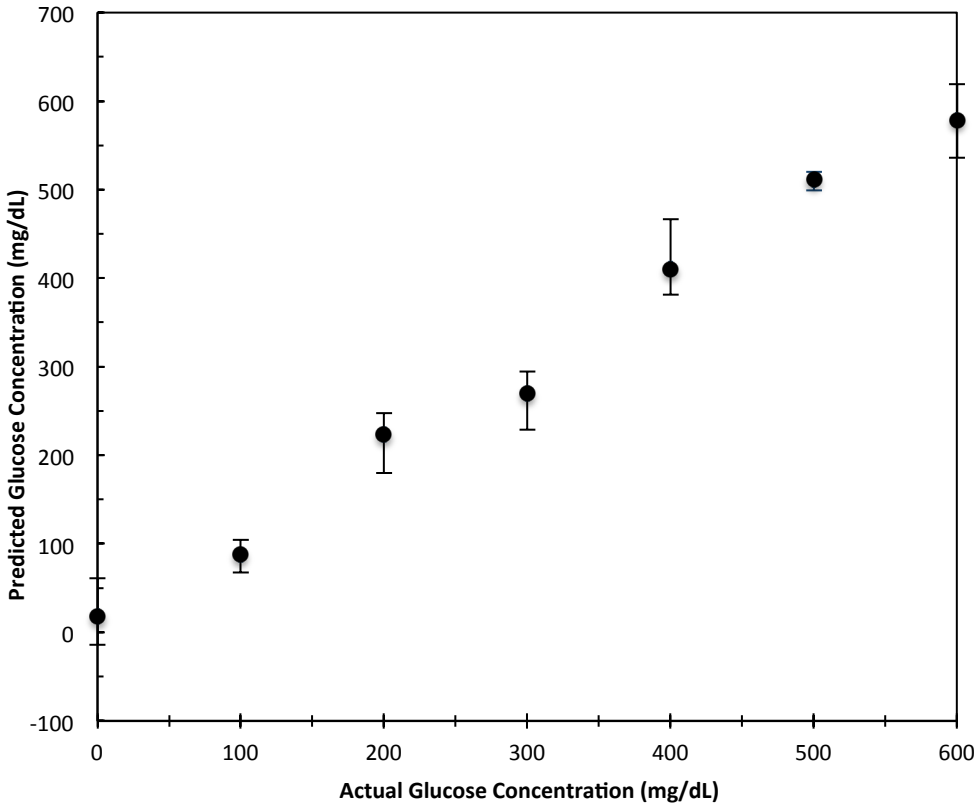

Figure 16. Predicted glucose concentration as a function of actual glucose concentration of 0-600 mg/dL for 635 nm wavelength with time-variant motion.

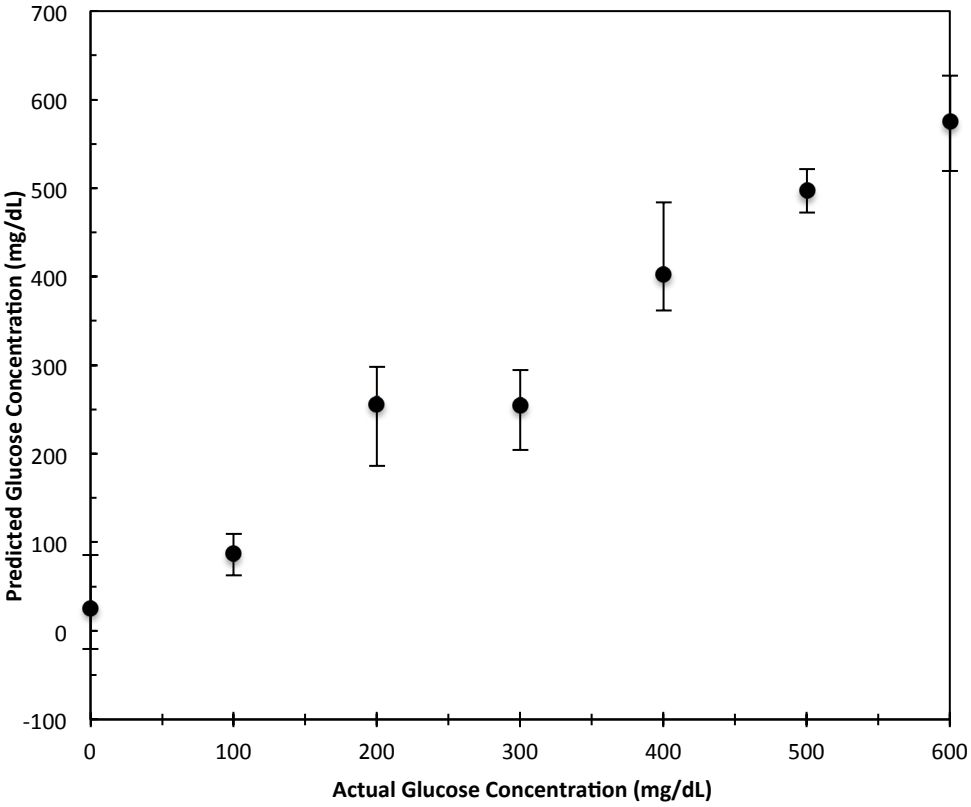

Figure 17. Predicted glucose concentration as a function of actual glucose concentration of 0-600 mg/dL for 830 nm wavelength with time-variant motion.

In the presence of motion and the resulting time-varying birefringence, a simple linear regression first provided error for each wavelength. The mean error for glucose prediction using the 635 nm and 830 nm wavelengths were 39.9 and 59.9 mg/dL respectively, or an average of 49.9 mg/dL error (74). The correlation coefficients for glucose prediction using the 635 nm and 830 nm wavelengths were 0.970 and 0.935 respectively. Multiple-linear regression analysis was applied to predict and essentially subtract out the contribution of birefringence from the total rotation of the two wavelengths' polarization state. The MLR approach reduced the error to 25.7 mg/dL with a correlation coefficient of 0.990 shown in **Figure 18** (74). This error was larger than previous works (76), because the 635 nm wavelength error was large before motion was added. The study without motion showed 20.3 mg/dL error with the 635 nm wavelength. The MLR approach could not reduce noise if the noise wasn't correlated between the two wavelengths. The third goal reduced system components and therefore increased sensitivity.

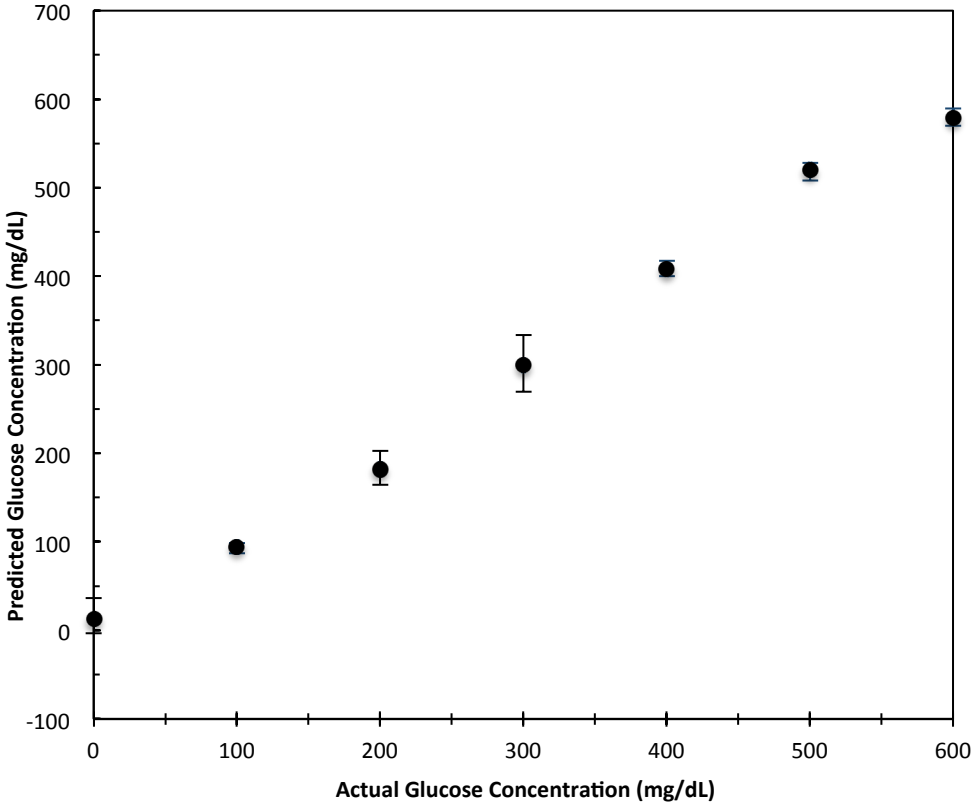

Figure 18. Predicted glucose concentration as a function of actual glucose concentration of 0-600 mg/dL with time-variant motion after MLR analysis.

These results show a decrease in system response time over the real-time dual-wavelength approach presented by Malik et al. Their slower modulation frequency (1.09 kHz) and their software based (not FPGA based) PID control feedback system required ~100 msec for system stabilization (39). The high-speed approach combined a faster modulation frequency (37 kHz) and a faster FPGA based PID control feedback system for a faster 10 msec system stabilization time. It, therefore, follows that the high-speed approach was ~10 times faster.

Concluding Statement for the Single Faraday Modulation Frequency Approach

In summary, the integration of a high-speed ferrite based Faraday rotator into the dual-wavelength polarimeter was accomplished and *in vitro* phantom studies were performed with and without motion artifact. The stabilization time was shown to be less than 10 msec, and standard errors were less than 26 mg/dL. The faster Faraday modulation improved the slow filtering process and improved the stabilization time in the closed-loop response of the sensor. In the third goal (described in the next section), an attempt was made to reduce the 26 mg/dL error and increase the speed even further by the removal of system components.

Goal 3: Dual-Wavelength Polarimeter with Dual Ferrite Core Faraday Modulators

For the third research goal, the two signals riding on the two different wavelengths were separated electronically with lock-in amplifiers, rather than optically with filters, to remove overall system components. Specifically, a beam splitter, two filters, a photodiode, and a photodiode amplifier were removed. The Faraday rotator also included DC-compensation for closed-loop feedback onto the same ferrite core Faraday rotator that was already modulating linearly polarized light. As a result, two Faraday rotators that could modulate and compensate replaced the three Faraday rotators used in the second research goal. The simplified sensor was then characterized *in vitro* with and without motion artifact to evaluate system error.

Sensitivity Experiments

The simplified dual-wavelength polarimeter utilizing dual Faraday modulation for glucose sensing was designed. The design operated at frequencies within the 30 to 75 kHz region of interest. Specifically, the design operated at 52.2 and 73.5 kHz with modulation and compensation on a single crystal. The faster modulation frequency allowed for a faster stabilization time than previous air-core systems.

For data processing without motion, a linear regression model of the data acquired from the high-speed dual-wavelength polarimeter provided a standard error of 8.51 and 15.1 mg/dL for the 635 and 532 nm wavelengths respectively. As previously stated, the 830 nm wavelength laser from the second goal was switched to the 532 nm wavelength for this goal, because the 532 nm wavelength laser creates a larger rotation

due to optical activity and Faraday effect than the 830 nm wavelength laser. The 635 and 532 nm wavelengths provided correlation coefficients of 0.999 and 0.995 respectively. **Figure 19** shows a MLR of the results of three tests and their errors corresponding to various glucose concentrations ranging from 0-600 mg/dL with 100 mg/dL intervals. The MLR improved the standard error and correlation coefficient of the data without motion to 7.89 mg/dL and 0.999.

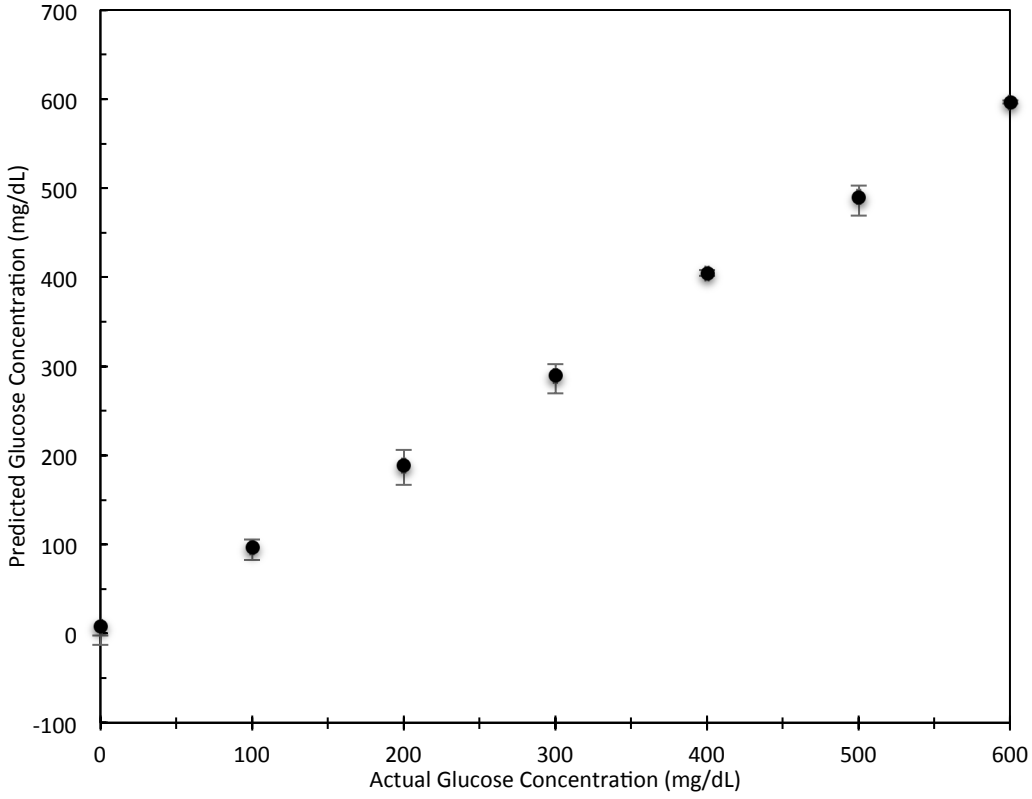

Figure 19. Predicted glucose concentration as a function of actual glucose concentration for 635 nm and 532 nm dual-wavelength approach from 0-600 mg/dL without motion.

52.2 kHz and 73.6 kHz modulation frequencies are roughly twice the frequency used for the second research goal. As a result, the lock-in amplifiers could filter with faster 100 usec time constants (as opposed to 1 msec time constants used in the single frequency experiments reported in the second goal), and the FPGA-based dual-wavelength system could stabilize as fast as ~2 msec (as opposed to ~10 msec from the single frequency experiments). **Figure 20** shows the stabilization time for the 635 nm (red) wavelength. The recorded feedback voltage began to stabilize at ~3.5465 seconds and completely stabilized by ~3.5485 seconds. The PID built with the FPGA had an acquisition rate of 100 usec. Any acquisition rate faster than 100 usec produced unstable results.

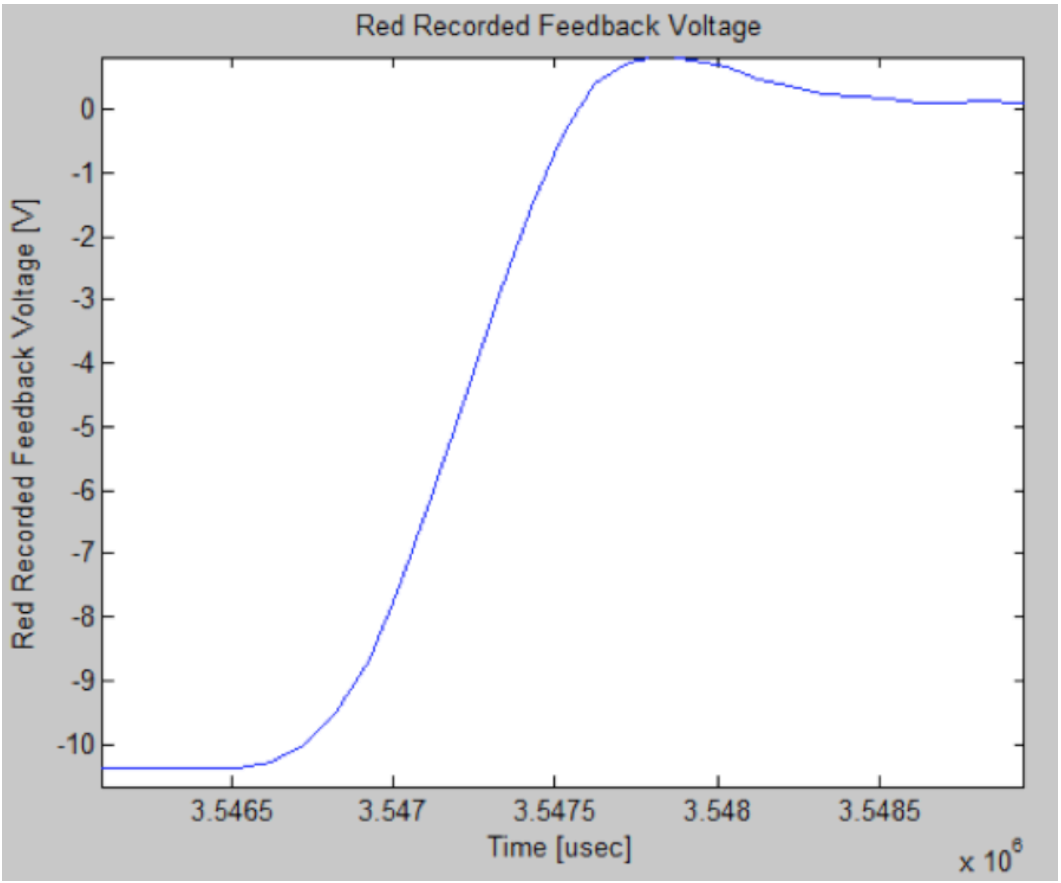

Figure 20. Stabilization time for the closed-loop dual-wavelength optical polarimeter to sense glucose.

Experiments with Motion Artifact

Similar to the results without motion, the dual-frequency dual-wavelength polarimetric approach functioned within a target range of 0-600 mg/dL glucose concentration with a target error equivalent to the air-core system in the presence of motion artifact of ideally less than 15 mg/dL. Glucose concentrations between 0-600 mg/dL with 100 mg/dL increments determined the sensor's repeatability and accuracy in the presence of motion artifact. **Figures 21** and **22** show the predicted glucose concentrations as a function of the actual glucose concentrations for wavelengths 635 nm and 532 nm. A simple regression analysis showed that the mean error for glucose prediction using the 635 nm and 532 nm wavelengths were 19.6 and 63.5 mg/dL respectively, in the presence of motion and the resulting time-varying birefringence. The 635 nm and 532 nm wavelengths provided correlation coefficients of 0.993 and 0.916. Similar to Malik et al., MLR analysis was applied to minimize the contribution of birefringence from the total rotation of the two wavelengths' polarization state (39). The MLR approach reduced the error to 13.0 mg/dL with a correlation coefficient of 0.997 as shown in **Figure 23**.

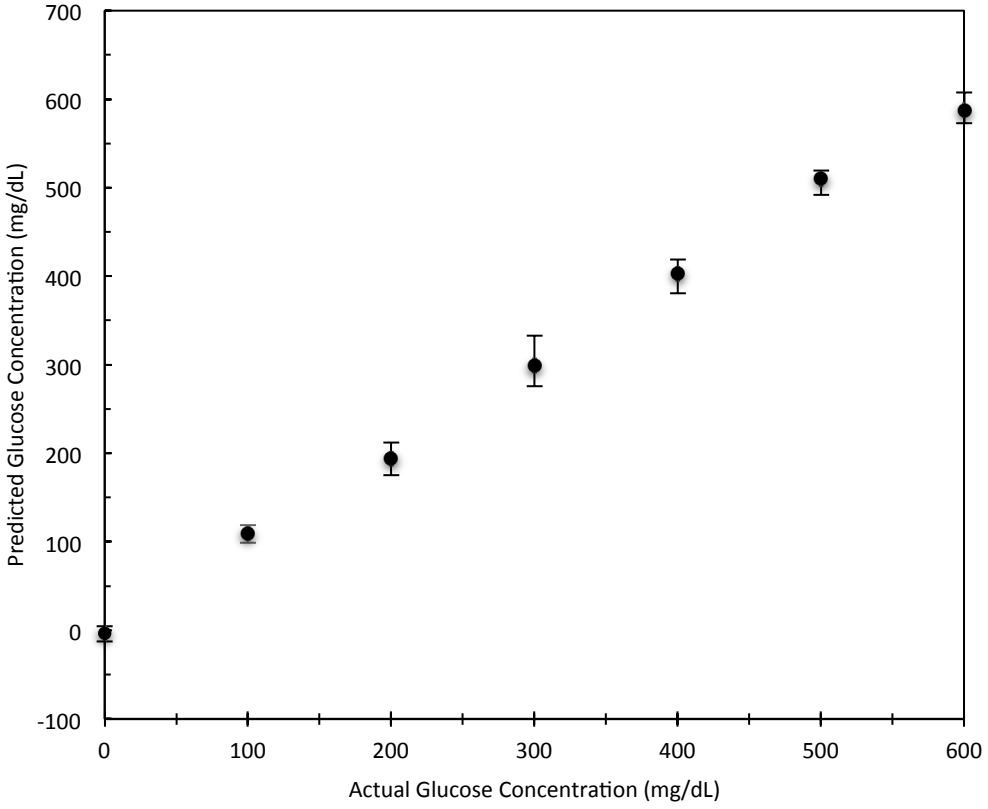

Figure 21. Predicted glucose concentration as a function of actual glucose concentration of 0-600 mg/dL for 635 nm wavelength with time-variant motion.

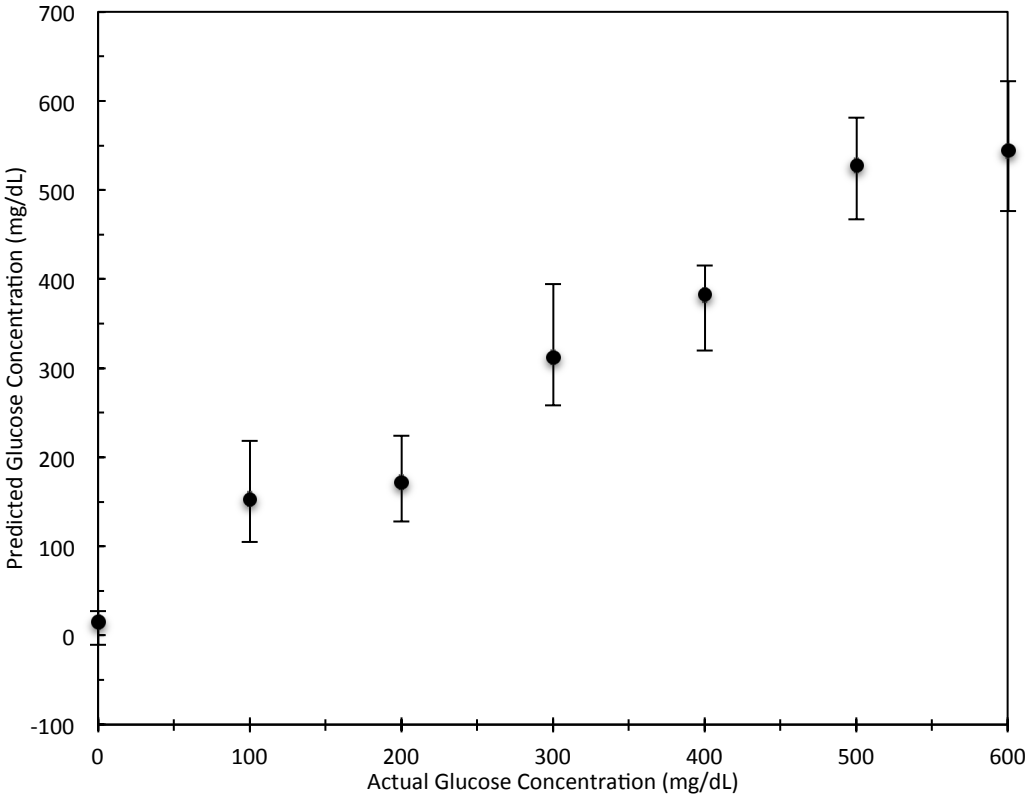

Figure 22. Predicted glucose concentration as a function of actual glucose concentration of 0-600 mg/dL for 532 nm wavelength with time-variant motion.

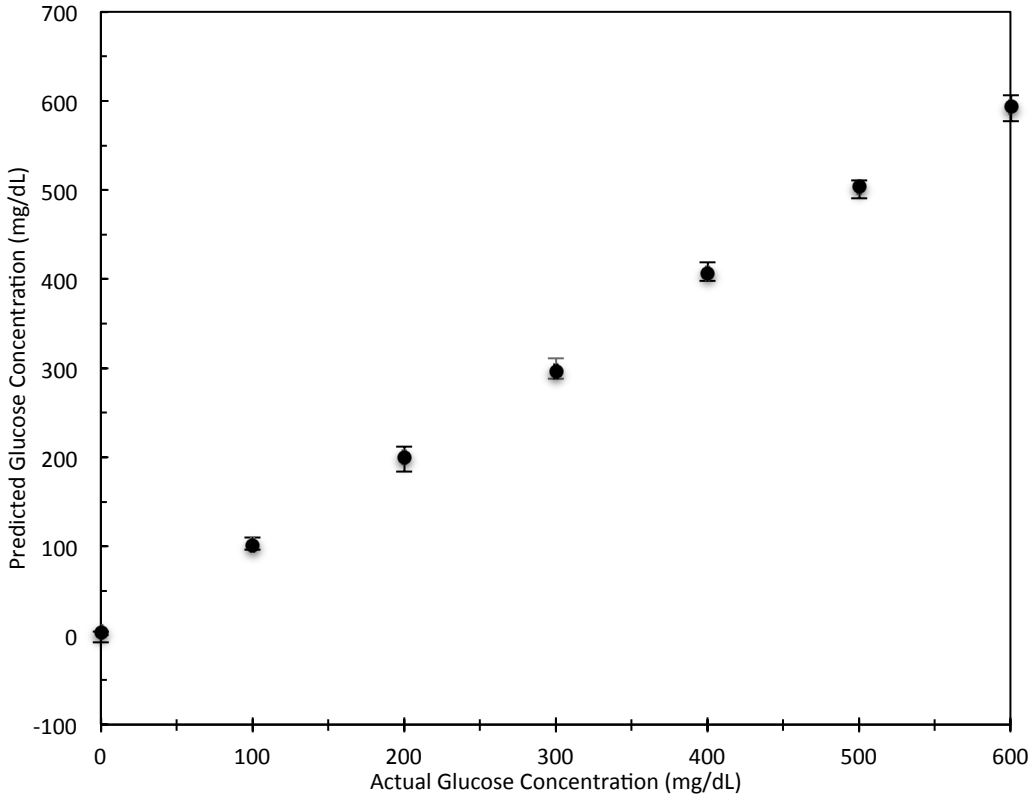

Figure 23. Predicted glucose concentration as a function of actual glucose concentration of 0-600 mg/dL with time-variant motion after MLR analysis.

Concluding Statement for the Dual-Frequency Faraday Modulation Approach

In summary, overall system components were removed by separating the two signals riding on the two different wavelengths electronically with lock-in amplifiers, rather than optically with filters. The modulation frequencies of 52.2 and 73.6 kHz allowed for a faster stabilization time than previous air-core systems.

CHAPTER V

CONCLUSIONS

For the first research goal, a high-frequency, ferrite core Faraday rotator – that modulated and rotated linearly polarized light in a frequency range of 30 to 75 kHz – was effectively developed. This rotator was made to work by wrapping 100 turns of 125/40 litz wire around a C-shaped ferrite core for AC-modulation and 20 turns of 24-gauge wire around TGG crystal for DC-compensation.

For the second goal, a high-speed ferrite based Faraday rotator was integrated into the dual-wavelength polarimeter. *In vitro* phantom studies were performed with and without motion artifact, with stabilization times less than 10 msec and standard errors less than 26 mg/dL in the presence of motion. The faster Faraday modulation improved the slow filtering process as well as the stabilization time in the closed-loop response of the sensor. The 635 nm wavelength error was large before motion was added. The study without motion showed 20.3 mg/dL error with the 635 nm wavelength. The MLR approach could not reduce noise if the noise was not correlated between the two wavelengths.

For the third goal, system components were reduced to improve sensitivity. In particular, signal separation was accomplished using an electronic method (as opposed to optically with filters), which ultimately resulted in the removal of unnecessary parts (one beam splitter, one Faraday rotator, two filters, one photodiode, and one phodiode amplifier). This approach used two modulation frequencies instead of one, provided

simplicity, and reduced the overall system cost. Moreover, the dual-Faraday modulation method reduced error to 13.0 mg/dL in the presence of motion. A higher modulation frequency and a faster lock-in amplifier reduced the overall system stabilization time from ~100 msec obtained in the air core approach to ~10 msec obtained in the single Faraday modulation approach and finally to ~2 msec obtained in the dual Faraday modulation approach.

REFERENCES

1. U.S. Department of Health and Human Services, "National diabetes fact sheet: national estimates and general information on diabetes and prediabetes in the United States," (2011), Date Accessed: 02/01/2015, http://www.cdc.gov/diabetes/pubs/pdf/ndfs_2011.pdf.

2. Centers for Disease Control and Prevention, "National diabetes statistics report," (2014), Date Accessed: 02/01/2015, http://www.cdc.gov/diabetes/pubs/statsreport14/national-diabetes-report-web.pdf.

3. Diabetes Digital Media, "Diabetes and hyperglycemia - hyperglycemia symptoms and causes," (2014), Date Accessed: 02/01/2015, http://www.diabetes.co.uk/Diabetes-and-Hyperglycaemia.html.

4. Diabetes Digital Media, "Hypoglycemia - symptoms, causes and treatment," (2014), Date Accessed: 02/01/2015, http://www.diabetes.co.uk/Diabetes-and-Hypoglycaemia.html.

5. M. Blumenkranz, "The effect of intensive treatment of diabetes on the development and progression of long-term complications in insulin-dependent diabetes mellitus," *N Engl J Med* **329**(14), 977-986 (1993).

6. G. S. Wilson, and Y. Zhang, "Introduction to the glucose sensing problem," *In Vivo Glucose Sensing*, pp. 1-27, John Wiley & Sons, Inc., Hoboken, New Jersey (2009).

7. L. C. Clark, and C. Lyons, "Electrode systems for continuous monitoring in cardiovascular surgery," *Annals of the New York Academy of Sciences* **102**(1), 29-45 (1962).

8. S. J. Updike, and G. P. Hicks, "The enzyme electrode," *Nature* **214**(5092), 986-988 (1967).

9. A. E. G. Cass et al., "Ferrocene-mediated enzyme electrode for amperometric determination of glucose," *Analytical Chemistry* **56**(4), 667-671 (1984).

10. A. Caduff et al., "Non-invasive glucose monitoring in patients with Type 1 diabetes: a Multisensor system combining sensors for dielectric and optical characterisation of skin," *Biosensors & Bioelectronics* **24**(9), 2778-2784 (2009).

11. I. Ermolina, Y. Polevaya, and Y. Feldman, "Analysis of dielectric spectra of eukaryotic cells by computer modeling," *European Biophysics Journal : EBJ* **29**(2), 141-145 (2000).

12. Y. Polevaya et al., "Time domain dielectric spectroscopy study of human cells. II. Normal and malignant white blood cells," *Biochim Biophys Acta* **1419**(2), 257-271 (1999).

13. A. Caduff et al., "First human experiments with a novel non-invasive, non-optical continuous glucose monitoring system," *Biosensors & Bioelectronics* **19**(3), 209-217 (2003).

14. M. Gourzi et al., "Non-invasive glycaemia blood measurements by electromagnetic sensor: study in static and dynamic blood circulation," *Journal of Medical Engineering & Technology* **29**(1), 22-26 (2005).

15. A. Tura et al., "A low frequency electromagnetic sensor for indirect measurement of glucose concentration: in vitro experiments in different conductive solutions," *Sensors (Basel, Switzerland)* **10**(6), 5346-5358 (2010).

16. G. R. Moran et al., "A dielectric analysis of liquid and glassy solid glucose/water solutions," *Carbohydrate Research* **328**(4), 573-584 (2000).

17. H. Melikyan et al., "Non-invasive in vitro sensing of D-glucose in pig blood," *Medical Engineering & Physics* **34**(3), 299-304 (2012).

18. O. S. Khalil, "Noninvasive photonic-crystal material for sensing glucose in tears," *Clin Chem* **50**(12), 2236-2237 (2004).

19. E. A. Moschou et al., "Fluorescence glucose detection: advances toward the ideal in vivo biosensor," *J Fluoresc* **14**(5), 535-547 (2004).

20. H. von Lilienfeld-Toal et al., "A novel approach to non-invasive glucose measurement by mid-infrared spectroscopy: The combination of quantum cascade lasers (QCL) and photoacoustic detection," *Vibrational Spectroscopy* **38**(1–2), 209-215 (2005).

21. H. M. Heise, A. Bittner, and R. Marbach, "Clinical chemistry and near infrared spectroscopy: technology for non-invasive glucose monitoring," *Journal of Near Infrared Spectroscopy* **6**(4), 349-359 (1998).

22. H. M. Heise, and R. Marbach, "Human oral mucosa studies with varying blood glucose concentration by non-invasive ATR-FT-IR-spectroscopy," *Cellular and Molecular Biology (Noisy-le-Grand, France)* **44**(6), 899-912 (1998).

23. H. W. Siesler et al., *Near-Infrared Spectroscopy: Principles, Instruments, Applications* W. Wiley-VCH, Ed. (2002).

24. R. Raghavachari, *Near-Infrared Applications in Biotechnology*, New York, New York (2001).

25. K. Maruo, M. Tsurugi, and J. Chin, "Noninvasive blood glucose assay using a newly developed near-infrared system," *IEEE J Sel Top Quant* **9**(2), 322-330 (2003).

26. M. A. Arnold, and G. W. Small, "Noninvasive glucose sensing," *Anal Chem* **77**(17), 5429-5439 (2005).

27. K. V. Larin et al., "Noninvasive blood glucose monitoring with optical coherence tomography," *Diabetes Care* **25**(12), 2263-2267 (2002).

28. S. J. Yeh, C. F. Hanna, and O. S. Khalil, "Monitoring blood glucose changes in cutaneous tissue by temperature-modulated localized reflectance measurements," *Clin Chem* **49**(6 Pt 1), 924-934 (2003).

29. A. J. Berger et al., "Multicomponent blood analysis by near-infrared Raman spectroscopy," *Applied Optics* **38**(13), 2916-2926 (1999).

30. E. B. Hanlon et al., "Prospects for in vivo Raman spectroscopy," *Phys Med Biol* **45**(2), R1-59 (2000).

31. A. Sieg, R. H. Guy, and M. B. Delgado-Charro, "Noninvasive glucose monitoring by reverse iontophoresis in vivo: application of the internal standard concept," *Clin Chem* **50**(8), 1383-1390 (2004).

32. S. Lee et al., "Glucose measurements with sensors and ultrasound," *Ultrasound in Medicine & Biology* **31**(7), 971-977 (2005).

33. H. A. MacKenzie et al., "Advances in photoacoustic noninvasive glucose testing," *Clin Chem* **45**(9), 1587-1595 (1999).

34. W. F. March, B. Rabinovitch, and R. L. Adams, "Noninvasive glucose monitoring of the aqueous humor of the eye: part II. animal studies and the scleral lens," *Diabetes Care* **5**(3), 259-265 (1982).

35. B. Rabinovitch, W. F. March, and R. L. Adams, "Noninvasive glucose monitoring of the aqueous humor of the eye: part I. measurement of very small optical rotations," *Diabetes Care* **5**(3), 254-258 (1982).

36. T. W. King et al., "Multispectral polarimetric glucose detection using a single Pockels cell," *Optical Engineering* **33**(8), 2746-1753 (1994).

37. R. W. Knighton, X. R. Huang, and L. A. Cavuoto, "Corneal birefringence mapped by scanning laser polarimetry," *Opt. Express* **16**(18), 13738-13751 (2008).

38. B. H. Malik, and G. L. Coté, "Real-time, closed-loop dual-wavelength optical polarimetry for glucose monitoring," *Journal of Biomedical Optics* **15**(1), 017002 (2010).

39. B. H. Malik, C. W. Pirnstill, and G. L. Cote, "Dual wavelength polarimetric glucose sensing in the presence of birefringence and motion artifact using anterior chamber of the eye phantoms," pp. 1-27, *Journal of Biomedical Optics* (2012).

40. G. Purvinis, B. D. Cameron, and D. M. Altrogge, "Noninvasive polarimetric-based glucose monitoring: an in vivo study," *Journal of Diabetes Science and Technology* **5**(2), 380-387 (2011).

41. Q. Wan, G. L. Coté, and J. B. Dixon, "Dual-wavelength polarimetry for monitoring glucose in the presence of varying birefringence," *Journal of Biomedical Optics* **10**(2), 024029 (2005).

42. G. L. Cote, M. D. Fox, and R. B. Northrop, "Noninvasive optical polarimetric glucose sensing using a true phase measurement technique," *Biomedical Engineering, IEEE Transactions on* **39**(7), 752-756 (1992).

43. B. D. Cameron, and G. L. Cote, "Noninvasive glucose sensing utilizing a digital closed-loop polarimetric approach," *Biomedical Engineering, IEEE Transactions* **44**(12), 1221-1227 (1997).

44. C. Chou et al., "Noninvasive glucose monitoring in vivo with an optical heterodyne polarimeter," *Appl. Opt.* **37**(16), 3553-3557 (1998).

45. B. D. Cameron, J. S. Baba, and G. L. Coté, "Measurment of the glucose transport time delay between the blood and aqeuous humor of the eye for the eventual development of a noninvasive glucose sensor," *Diabetes Technology & Therapeutics* **3**(2), 201-207 (2001).

46. B. D. Cameron et al., "The Use of Polarized Laser Light Through the Eye for Noninvasive Glucose Monitoring," *Diabetes Technology & Therapeutics* **1**(2), 135-143 (1999).

47. A. J. Webb, and B. D. Cameron, "The use of optical polarimetry as a noninvasive in vivo physiological glucose monitor," R. J. Nordstrom, and G. L. Cote, Eds. 79060E-79065 (2011).

48. C. F. So et al., "Recent advances in noninvasive glucose monitoring," *Medical Devices (Auckland, N.Z.)* **5**(45-52 (2012).

49. M. J, *Organic Chemistry*, 3 ed., Brooks/Cole Publishing Company, Pacific Grove, CA (1992).

50. M. A. Melin, "On the manufacture of sugare in Belgium," *ARCHIVE: Proceedings of the Institution of Mechanical Engineers* **34**(368-420 (1883).

51. E. J. Gillham, "Photoelectric polarimeter using the Faraday effect," *Nature* **178**(1412-1413 (1956).

52. G. L. Cote, "Development of a robust optical glucose sensor," University of Connecticut, Storrs, CT (1990).

53. M. J, Goetz, "Microdegree polarimetry for glucose detection," University of Connecticut, Storrs, CT (1992).

54. M. J. Goetz, M. D. Fox, and R. B. Northrop, "Microdegree polarimetry using a diode laser for glucose detection," *Bioengineering Conference, 1992., Proceedings of the 1992 Eighteenth IEEE Annual Northeast* 97 (1992).

55. M. Michael, "Multi-spectral glucose sensing using a polarimetric differencing technique," Texas A&M University, College Station, TX (1995).

56. G. L. Cote et al., "Multispectral polarimetric system for glucose monitoring," *SPIE Photonics West* 36-40 (1998).

57. R. R. Ansari, S. Bockle, and L. Rovati, "New optical scheme for a polarimetric-based glucose sensor," *J Biomed Opt* **9**(1), 103-115 (2004).

58. R. Rawer, W. Stork, and K. D. Muller-Glaser, "Polarimetric methods for measurement of intra ocular glucose concentration," *Biomedizinische Technik. Biomedical Engineering* **47 Suppl 1 Pt 1**(186-188 (2002).

59. R. Rawer, W. Stork, and C. F. Kreiner, "Non-invasive polarimetric measurement of glucose concentration in the anterior chamber of the eye," *Graefe's Archive for Clinical and Experimental Ophthalmology = Albrecht Von Graefes Archiv fur Klinische und Experimentelle Ophthalmologie* **242**(12), 1017-1023 (2004).

60. B. D. Cameron, and H. Anumula, "Development of a real-time corneal birefringence compensated glucose sensing polarimeter," *Diabetes Technology & Therapeutics* **8**(2), 156-164 (2006).

61. C. W. Pirnstill et al., "In vivo glucose monitoring using dual-wavelength polarimetry to overcome corneal birefringence in the presence of motion," *Diabetes Technol Ther* **14**(9), 819-827 (2012).

62. C. W. Pirnstill, D. Grunden, and G. L. Coté, "Polarimetric glucose sensing in vitro: a high frequency approach," *SPIE Photonics West* 859101-859101-859107 (2013).

63. Prentice-Hall, Inc., "Schematic of a Polarimeter," (2002), Date Accessed: 02/01/2015, http://wps.prenhall.com/wps/media/objects/724/741576/chapter_05.html.

64. R. C. Jones, "A new calculus for the treatment of optical systems," *J. Opt. Soc. Am.* **31**(7), 488-493 (1941).

65. M. J. Goetz Jr, "Microdegree polarimetry for glucose detection," The University of Connecticut, Storrs, CT (1993).

66. L. Pasteur, *Researches on the molecular asymmetry of natural organic products*, Alembic Club, Edinburgh, UK (1905).

67. S. Krimm, "Fundamental aspects and recent developments in optical rotatory dispersion and circular dichroism," *Journal of Polymer Science: Polymer Letters Edition* **12**(6), 360-361 (1974).

68. D. Bobbitt, "Improvements in detectabilities in polarimeters using high-frequency modulation," *Applied Spectroscopy* **40**(3), 407-410 (1986).

69. Y.-L. Lo et al., "Full-field heterodyne polariscope with an image signal processing method for principal axis and phase retardation measurements," *Applied Optics* **45**(31), 8006-8012 (2006).

70. C. W. Pirnstill et al., "Design and characterization of a ferromagnetic, air gapped magneto-optic Faraday rotator," *Optics Letters* **38**(8), 1298-1300 (2013).

71. S. J. Chapman, *Electric Machinery Fundamentals*, 3 ed., McGraw-Hill, New York, New York (2003).

72. Magnetic Materials Producers Association, "Soft ferrites: a user's guide," (1997), Date Accessed: 02/01/2015, http://www.magneticsgroup.com/pdf/mmpa SFG-98.pdf.

73. F. E. Terman, *Radio engineers' handbook*, McGraw-Hill, New York, New York (1943).

74. D. T. Grunden, C. W. Pirnstill, and G. L. Coté, "High-speed dual-wavelength optical polarimetry for glucose sensing," *SPIE Photonics West* 895111-895111-895116 (2014).

75. B. H. Malik, and G. L. Coté, "Characterizing dual wavelength polarimetry through the eye for monitoring glucose," *Biomed. Opt. Express* **1**(5), 1247-1258 (2010).

76. B. H. Malik, C. W. Pirnstill, and G. L. Cote, "Polarimetric glucose sensing in an artificial eye anterior chamber," R. J. Nordstrom, and G. L. Cote, Eds., *SPIE Photonics West* 82290O-82290O-82296 (2012).